

Error Approximation and Bias Correction in Dynamic Problems using a Recurrent Neural Network/Finite Element Hybrid Model

Moritz von Tresckow^{a,*}, Herbert De Gersem^a, Dimitrios Loukrezis^a

^a *Technische Universität Darmstadt, Institute for Accelerator Science and Electromagnetic Fields (TEMF), Schlossgartenstr. 8, 64289 Darmstadt, Germany*

Abstract

This work proposes a hybrid modeling framework based on recurrent neural networks (RNNs) and the finite element (FE) method to approximate model discrepancies in time dependent, multi-fidelity problems, and use the trained hybrid models to perform bias correction of the low-fidelity models. The hybrid model uses FE basis functions as a spatial basis and RNNs for the approximation of the time dependencies of the FE basis' degrees of freedom. The training data sets consist of sparse, non-uniformly sampled snapshots of the discrepancy function, pre-computed from trajectory data of low- and high-fidelity dynamic FE models. To account for data sparsity and prevent overfitting, data upsampling and local weighting factors are employed, to instigate a trade-off between physically conforming model behavior and neural network regression. The proposed hybrid modeling methodology is showcased in three highly non-trivial engineering test-cases, all featuring transient FE models, namely, heat diffusion out of a heat sink, eddy-currents in a quadrupole magnet, and sound wave propagation in a cavity. The results show that the proposed hybrid model is capable of approximating model discrepancies to a high degree of accuracy and accordingly correct low-fidelity models.

Keywords: Bias Correction, Dynamic Problems, Finite Elements, Hybrid Modeling, Model Error Approximation, Multi-Fidelity Modeling, Recurrent Neural Networks

^{*}Corresponding author: moritz.von_tresckow@tu-darmstadt.de

1. Introduction

Over the last decade, machine learning (ML) has established itself as one of the prime research subjects in the contemporary sciences, finding applications in biology [1], engineering [28, 44, 62], physics [9, 27], and medicine [67], to name only a few areas. Even though this development can to some extent be attributed to hype [59], there are domains in which ML methods have outperformed state-of-the-art techniques. Explicit examples include the development of convolutional neural networks (CNNs) and graph neural networks for image classification [11, 42, 66], large language models for natural language processing [47], and deep reinforcement learning for applications in autonomous driving [56]. However, ML models are subjected to the curse of dimensionality and training often involves solving nonlinear optimization problems which causes training times to be a significant concern. Nevertheless, with processing units such as CPUs and GPUs becoming more performant each year [7], the impact of ML will most likely increase even further.

On the basis of these recent successes, ML quickly penetrated traditional scientific computing methods [30]. Recent advances in this area lie in the emergence of physics-informed neural networks (PINNs) [8, 22, 29], hybrid modeling [34, 41], but also in the field of data-driven computing [18, 33]. PINNs incorporate physics-based loss functions to train neural networks (NNs) to exhibit physically conforming behavior, hybrid modeling approaches seek to combine "the best of both worlds", and data-driven computing methods extend traditional numerical approximation methods for partial differential equations (PDEs) to directly incorporate measurement data. Worthy of note, however, is that ML does not always improve upon established methods and its success or lack thereof significantly depends on the problem setting to which it is applied [43]. For instance, deep learning inherently requires nonlinear optimization and is at a natural disadvantage when competing with traditional solvers in low dimensional, linear problem settings, consequently requiring nonlinear and/or high-dimensional problems problem settings to achieve a computational benefit [16].

In the authors' opinion, data-based bias correction and model validation, a framework discussed in detail in the recent work of Levine and Stuart [37], provides exactly such a setting. In particular, let us consider the case of multi-fidelity modeling, where computationally inexpensive, low-fidelity models are employed to approximate time- and resource-demanding high-fidelity models,

resulting in a model hierarchy according to accuracy and computational cost [1, 48, 50]. Bias correction and model validation occur naturally in multi-fidelity modeling. In bias correction, a corrective term is computed, which accounts for the discrepancy between models of different fidelity [50]. In model validation, the accuracy of the low-fidelity model is validated against a reference [46, 54, 55]. In both cases, approximating the systematic error, also referred to as model bias or discrepancy, is necessary. Primary approaches for learning a discrepancy function include Bayesian inference [12, 13, 38, 64] and Gaussian processes [3, 32, 19, 38, 49]. In more recent years, bias correction by means of neural networks has also been attempted [36, 45, 63]. Specifically, Um et al. [61] successfully calculate a correction term for a fluid flow simulation by integrating the solver directly into the training loop of a CNN. Nevertheless, this approach, calculates a correction operator and not the discrepancy function itself.

In this work, we approximate the discrepancy functions between low and high-fidelity finite element (FE) simulations of dynamical systems, by employing a recurrent neural network (RNN)/FE-based hybrid model, which is trained on sparse, non-uniformly sampled trajectory data of the high-fidelity solution. The high and low-fidelity simulations differ by choice of computational mesh and modeling assumptions, consequently inducing both discretization and modeling errors. Similarly, the RNN/FE-based hybrid model is constructed by splitting spatial and temporal dependencies. To account for the sparsity of the training data and prevent the overfitting phenomenon, the training data is upsampled artificially using linear interpolation operators and localized Gaussian priors at missing time steps to provide noise stabilization, an approach commonly used in game design and image processing [26, 31, 51]. Local weighting factors on the training data are also employed to control the interpolation behavior of the model. The hybrid model is applied to three engineering-relevant test cases, namely, heat diffusion out of a heat sink, eddy-currents in a quadrupole magnet, and sound wave propagation in a cavity. The results show that the proposed hybrid model and training regimen is capable of approximating model discrepancies to a high degree of accuracy.

The main contribution of this work lies in the application of RNNs for discrepancy function approximation in the setting of multi-fidelity modeling and simulation, in combination with the FE method. Even though surrogate modeling has been used extensively to approximate high-fidelity simulations [14, 10, 21], using RNNs to learn model errors has been first proposed in

[37], however, not in combination with FE-based models and with only limited numerical experiments that do not include highly non-trivial engineering applications, as the ones available in the present work. Additional contributions concern the specific architecture of the hybrid model, as well as the treatment of hybrid model training with sparse data, such that the physically correct interpolation behavior is ensured.

The remaining of this paper provides, first, a theoretical overview of data-driven discrepancy approximation for model validation and bias correction (Section 2), followed by a presentation of the suggested hybrid modeling approach (Section 3), which highlights the hybrid model architecture and discusses the treatment of sparse training data. Numerical experiments showcasing the benefits of the proposed hybrid modeling approach are presented in Section 4. Last, concluding remarks and considerations for further methodological developments are available in Section 5.

2. Preliminaries and notation

2.1. Dynamical system simulation

The simulation of dynamical systems commonly requires the spatial and temporal discretization of an underlying boundary value problem (BVP), defined on $\Omega \times [0, T]$, where $\Omega \subset \mathbb{R}^d$ denotes the spatial domain at dimension $d \leq 3$ and $T \in \mathbb{R}_{\geq 0}$ the time range. Spatial discretization refers to the approximation of the system states by a finite dimensional basis representation and temporal discretization refers to state propagation along a discrete time axis. Therein, implicit time stepping schemes are frequently used, due to their advantages in numerical stability. The discrete dynamical system can be described by

$$\mathbf{x}_{t_{k+1}} = \Psi(\mathbf{x}_{t_{k+1}}, \mathbf{x}_{t_k}, t_{k+1}, t_k), \quad (1)$$

where $\Psi : \mathbb{R}^d \rightarrow \mathbb{R}^d$ is a time propagation operator and $\mathbf{x}_{t_k} : \Omega \rightarrow \mathbb{R}^d$ with $\mathbf{r} \mapsto \mathbf{x}_{t_k}(\mathbf{r})$, $\mathbf{r} \in \Omega$, are the system states at time $t = t_k$ where k is the time step indexing. In the case where the spatial discretization does not change over time, Ψ only operates on the degree of freedom (dof) of the states' basis coefficients. Accordingly, we can express (1) as $\hat{\mathbf{x}}_{t_{k+1}} = \Psi(\hat{\mathbf{x}}_{t_k})$ with $\Psi : \mathbb{R}^{N_{\text{dof}}} \rightarrow \mathbb{R}^{N_{\text{dof}}}$ and $\hat{\mathbf{x}} \in \mathbb{R}^{N_{\text{dof}}}$, where $N_{\text{dof}} \in \mathbb{N}$ denotes the number of spatial dof. Given an initial state \mathbf{x}_{t_0} , we can solve (1) for $N_T \in \mathbb{N}$ time steps of size $\Delta t \in \mathbb{R}$. The solution is an approximation of the states' trajectories,

the accuracy of which is dictated by the values of N_{dof} and N_T and the time stepping scheme. In this work, we focus on the FE method for spatial discretization and an implicit Euler scheme for time-stepping.

2.2. Model fidelity and discrepancy

Real-world scientific and engineering applications governed by dynamical problems are inherently complex, often requiring a large number of dof and time steps to be resolved to sufficient accuracy. Quite often, solution accuracy must be balanced against limitations in computational resources. A predominant factor in this trade-off is model fidelity, that is, the model's capability to precisely represent the physical system it approximates [17]. In the following, high- and low-fidelity models are denoted with Ψ_{hifi} and Ψ_{lofi} , respectively, as they will refer to dynamical system models, as they were introduced in Section 2.1. Accordingly, low- and high-fidelity system states at time t_k are respectively denoted with $\mathbf{x}_{t_k}^{\text{lofi}}$ and $\mathbf{x}_{t_k}^{\text{hifi}}$.

The difference in the results between a low- and a high-fidelity model can be predominantly attributed to a systematic error, which is commonly called model discrepancy or prediction bias. Model discrepancy can be quantified using a so-called discrepancy function $\delta_t : \mathbb{R}^d \rightarrow \mathbb{R}^d$ with $\delta_t(\mathbf{r}) = \mathbf{x}_t^{\text{hifi}}(\mathbf{r}) - \mathbf{x}_t^{\text{lofi}}(\mathbf{r})$, which maps the system state onto its corresponding systematic error [3, 40]. Non-systematic errors such as noise can similarly be expressed using an error function $\varepsilon_t : \mathbb{R}^d \rightarrow \mathbb{R}^d$, where a common assumption is $\varepsilon_t \sim \mathcal{N}(\mathbf{0}, \Sigma)$, $\Sigma \in \mathbb{R}^{d \times d}$. Under standard assumptions regarding the nature of the error and bias terms, for example, additivity or multiplicativity, the relationship between Ψ_{hifi} and Ψ_{lofi} can be expressed explicitly. For instance, under the additive bias and noise assumption, it holds that

$$\mathbf{x}_{t_k}^{\text{hifi}} = \mathbf{x}_{t_k}^{\text{lofi}} + \delta_{t_k} + \varepsilon_{t_k}, \quad (2)$$

for $k = 1, \dots, N_T$. Multiplicative or more complex relations are also possible. For the remaining of this work, we neglect the noise term in (2) and focus solely on the discrepancy function.

2.3. Data-driven discrepancy function approximation for model validation and correction

In the field of model validation, one is interested in whether the discrepancy function, δ_t , fulfills certain conditions, as to determine whether the use

of Ψ_{lofi} is justifiable [35]. In this context, a very general validation condition reads

$$\frac{1}{T} \int_{[0,T]} \|\delta_t\|_2^2 dt < C, \quad (3)$$

where $C > 0$ and $\|\cdot\|_2$ the $L^2(\Omega)$ norm. If δ_t fulfills (3), the use of Ψ_{lofi} is tenable [35]. To that end, the functional form of δ_{t_k} , which essentially quantifies the accuracy of Ψ_{lofi} with respect to Ψ_{hif} , must be inferred. While this could be accomplished by sufficiently sampling the high- and the low-fidelity models, the evaluation of the high-fidelity model must in many cases be avoided, typically due to its prohibitive computational cost. Instead, observed snapshot data $\mathbf{X} := \{\mathbf{x}_{t_k}^o\}_{t_k \in T_o}$, $T_o = \{t_k\}_{k=1}^{N_T}$, of its state trajectory may be available [37], for instance, originating from measurement setups or auxiliary simulations. To that end the superscript “o” is chosen to denote an observation.

Then, the validation of the low-fidelity model requires a parametric model δ_θ , which approximates the discrepancy based on the snapshots \mathbf{X} . This approximation can be accomplished with supervised learning algorithms. However, using data as a reference increases substantially the complexity of the validation problem, since \mathbf{X} might contain sparse, non-uniformly sampled, and noisy data. Possible remedies to this issue can be sought in novel physics-informed ML approaches, which integrate physics-inspired objective functions into the approximation process to induce physics conforming behavior in sparse data regimes [29]. Irrespective of the choice of the parametric model δ_θ and the multi-fidelity models, the minimization problem to be solved in order to determine an optimal parameter set θ^* given the training data set $\mathcal{D} := \{\mathbf{x}_{t_k}^o - \mathbf{x}_{t_k}^{\text{lofi}}\}_{t_k \in T_o}$, reads

$$\theta^* = \underset{\theta}{\operatorname{argmin}} \mathcal{J}_\theta, \text{ where } \mathcal{J}_\theta = \frac{1}{T} \int_0^T \|\delta_t - \delta_\theta\|_2 dt, \quad (4)$$

for $\delta_t \in \mathcal{D}$. The parametric model $\delta_\theta : \mathbb{R}^d \rightarrow \mathbb{R}^d$ for $\theta \in \mathbb{R}^{N_\theta}$, where N_θ denotes the number of parametric dof, can be chosen to map the low-fidelity states $\mathbf{x}_{t_k}^{\text{lofi}} \mapsto \delta_\theta$ onto the respective systematic error for all time instances $t_k \in T_o$ and points in the spatial domain $\mathbf{r} \in \Omega$ [61]. We note however, that this is one example and that other mappings are also possible.

Assuming a successful solution of the minimization problem (4), there are numerous uses for the function δ_{θ^*} . On the one hand, δ_{θ^*} can be used to

approximate the validation condition (3), ultimately verifying the low-fidelity model. On the other hand, it can be used to for bias correction, where we define a *corrected* system state

$$\mathbf{x}_{t_k}^{\text{corr}} = \mathbf{x}_{t_k}^{\text{lofi}} + \delta_{\theta^*}(\mathbf{x}_{t_k}^{\text{lofi}}), \quad (5)$$

where δ_{θ^*} models the discrepancy between the low-fidelity model and the reference data. The state trajectory resulting from (5) is the bias corrected trajectory of the low-fidelity model. In any case, model validation or correction depend significantly on the accuracy of the parametric model.

2.4. Modeling and discretization errors in transient finite element models

Multi-fidelity modeling and simulation introduces different types of systematic errors. In the particular case of FE analysis, these errors can be categorized into three different classes, namely, discretization errors, numerical errors, and modeling errors [5, 60]. Discretization errors occur when a function of a continuous variable is approximated by a finite dimensional basis representation, and primarily depend on the mesh resolution and the choice of the finite dimensional ansatz space. Reducing the discretization error requires a finer mesh resolution, thus increasing the number of dof. Numerical errors occur due to the finite precision of computation hardware, e.g., in the representation of real numbers as floating data types and the finite precision of iterative solvers. Truncation errors fall in the same category. Modeling errors occur due to assumptions and simplifications with respect to the problem itself. Common examples include misspecification of boundary conditions, incorrect definition of loading terms, linear approximations of otherwise nonlinear material responses, and 2D approximations of 3D geometries.

For the approximation of the discrepancy function between FE models of varying fidelity, a suitable representation basis must be chosen. Assuming solely the discretization error δ^d , a natural choice would be to use the FE basis functions. In the context of this work, we use the FE basis of the low-fidelity model Ψ_{lofi} , as we focus on bias correction. Consequently, a low-fidelity representation of the high-fidelity system states must be made available. Thus, it is necessary to define a projection operator $\mathcal{T} : \mathbb{R}^{N_{\text{dof}}^{\text{hifi}}} \rightarrow \mathbb{R}^{N_{\text{dof}}^{\text{lofi}}}$, where $N_{\text{dof}}^{\text{hifi}}$ and $N_{\text{dof}}^{\text{lofi}}$ denote the number of dof of the high- and the

low-fidelity model, respectively.¹ Assuming Ψ_{hifi} and Ψ_{lofi} to be defined on the same time grid, the discretization error at time step t_k is given as

$$\delta_{t_k}^{\text{d}} = \|\mathcal{T}(\mathbf{x}_{t_k}^{\text{hifi}}) - \mathbf{x}_{t_k}^{\text{lofi}}\|_2, \quad (6)$$

where $\mathbf{x}_{t_k}^{\text{hifi}} = \Psi_{\text{hifi}}(\mathbf{x}_{t_{k-1}}^{\text{hifi}})$ and $\mathbf{x}_{t_k}^{\text{lofi}} = \Psi_{\text{lofi}}(\mathbf{x}_{t_{k-1}}^{\text{lofi}})$ are the high-fidelity and low-fidelity states at time t .

On the other hand, modeling errors δ^{m} occur in the assumptions that define the BVP, ultimately affecting the definition of the time propagators. This fact is illustrated most clearly by assuming that Ψ_{hifi} and Ψ_{lofi} are parametrized by parameter sets $\lambda := (\lambda_1, \dots, \lambda_l)$, such that $\mathbf{x}_{t_k} = \Psi(\mathbf{x}_{t_{k-1}} | \lambda)$, and defined on the same computational mesh. Consequently, if $\lambda_{\text{hifi}} \neq \lambda_{\text{lofi}}$, the high-fidelity model $\mathbf{x}_{t_k}^{\text{hifi}} = \Psi(\mathbf{x}_{t_{k-1}}^{\text{hifi}} | \lambda_{\text{hifi}})$ and the low-fidelity model $\mathbf{x}_{t_k}^{\text{lofi}} = \Psi(\mathbf{x}_{t_{k-1}}^{\text{lofi}} | \lambda_{\text{lofi}})$ with $\mathbf{x}_{t_0}^{\text{hifi}} = \mathbf{x}_{t_0}^{\text{lofi}} = \mathbf{x}_{t_0}$. At each time step, this error can be quantified as

$$\delta_{t_k}^{\text{m}} = \|\mathbf{x}_{t_k}^{\text{hifi}} - \mathbf{x}_{t_k}^{\text{lofi}}\|_2. \quad (7)$$

In most multi-fidelity modeling settings, discretization and modeling errors are present simultaneously. Thus, a combined error term must be considered, which captures both. Considering (6) and (7), the combined error term can be quantified as

$$\delta_{t_k} = \|\mathcal{T}(\mathbf{x}_{t_k}^{\text{hifi}}) - \mathbf{x}_{t_k}^{\text{lofi}}\|_2, \quad (8)$$

where $\mathbf{x}_{t_k}^{\text{hifi}} = \Psi_{\text{hifi}}(\mathbf{x}_{t_{k-1}}^{\text{hifi}} | \lambda_{\text{hifi}})$ and $\mathbf{x}_{t_k}^{\text{lofi}} = \Psi_{\text{lofi}}(\mathbf{x}_{t_{k-1}}^{\text{lofi}} | \lambda_{\text{lofi}})$ with $\mathcal{T}(\mathbf{x}_{t_0}^{\text{hifi}}) = \mathbf{x}_{t_0}^{\text{lofi}}$. In the following sections, (8) provides the basis for preprocessing the training data.

3. Hybrid modeling methodology

3.1. Hybrid model elements and architecture

In the following section, we discuss the nature of the discrepancy function δ_t and our subsequent choice for the parametric model $\delta_\theta \approx \delta_t$. Discrepancy functions often display complex dynamics, exhibiting piecewise smooth and

¹Note that, when considering model validation, a projection $\mathcal{T} : \mathbb{R}^{N_{\text{dof}}^{\text{lofi}}} \rightarrow \mathbb{R}^{N_{\text{dof}}^{\text{hifi}}}$ is required, to get a high-fidelity representation of the low-fidelity states.

non-smooth behavior in the problem domain. These dynamics occur because discrepancy functions are required to capture harmonic propagating behavior, but also phase transitions, material interfaces, and interpolation errors. This phenomenon can be attributed to a variety of reasons, arising partially due to the underlying physics, but also due to the spatial and temporal discretization schemes, e.g., because of mesh inconsistencies or time stepping errors.

Considering these challenges, we split the approximation of time-dependent and spatially-dependent effects, such that an RNN is used to approximate the sequential, temporal dynamics, and the low-fidelity FE-basis functions are used to account for the spatial effects. As we seek to calculate a bias correction term for the low-fidelity model, we assume that the discrepancy function has the form

$$\delta_{t_k}(\mathbf{r}) = \sum_{i=1}^{N_{\text{dof}}^{\text{lofi}}} \hat{\delta}_{i,t_k} \phi_i(\mathbf{r}), \quad (9)$$

where $\hat{\delta}_{i,t_k}$ are the time dependent dof of the finite dimensional basis at time t_k and the i -th spatial dof, $\{\phi_i\}_{i=1}^{N_{\text{dof}}^{\text{lofi}}}$ are the basis functions of the low-fidelity model, and $\mathbf{r} \in \Omega$. We denote with $\hat{\boldsymbol{\delta}}_{t_k} := (\hat{\delta}_{1,t_k}, \dots, \hat{\delta}_{N_{\text{dof}}^{\text{lofi}},t_k})$ the vector containing the coefficients of (9).

The suggested hybrid modeling approach then consists of using the RNN to learn the time-dependent dof, $\hat{\boldsymbol{\delta}}_{t_k}$, at each time step. Due to their universal approximation property, as well as their use of residual connections to account for time-dependencies in the data, RNNs offer sufficient flexibility to approximate the dynamics in the data. In particular, a subcategory of RNNs called long-short term memory (LSTM) cells, are used to circumvent the vanishing gradient problem, by sharing information between the individual units and using hidden state variables to control the gating mechanism and shape information flow [25].

In our case, the RNN architecture itself comprises of two building blocks, namely a concatenation of LSTM cells and a linear output layer. A visualization is provided in Figure 1. In each training iteration, the RNN considers N_p consecutive time steps simultaneously, where the coefficients of the low-fidelity system states, \mathbf{x}_{t_k} , serve as inputs and the outputs approximate the discrepancy function's coefficients, $\hat{\boldsymbol{\delta}}_{t_k}$. We denote the mapping of the RNN

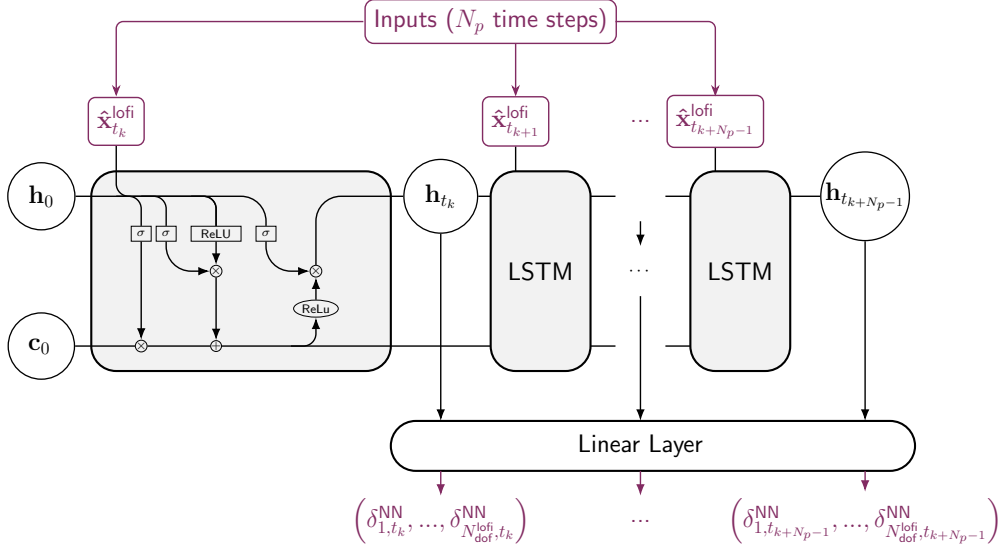


Figure 1: NN architecture comprising of LSTM units and a linear output layer used to approximate the coefficients of the discrepancy function. The vectors \mathbf{c}_t and \mathbf{h}_t , $t = t_k, \dots, t_{k+N_p-1}$, denote the cell states and hidden states of the LSTM units. The inputs and outputs are highlighted in purple.

with $\delta^{\text{NN}} : \mathbb{R}^{N_{\text{dof}}^{\text{lofi}}} \times \{t_k, \dots, t_{k+N_p-1}\} \rightarrow \mathbb{R}^{N_{\text{dof}}^{\text{lofi}}} \times \{t_k, \dots, t_{k+N_p-1}\}$, with

$$\delta^{\text{NN}}(\hat{\mathbf{x}}_{t_k}, \dots, \hat{\mathbf{x}}_{t_{k+N_p-1}}) = \{\delta_{t_k}^{\text{NN}}, \dots, \delta_{t_{k+N_p-1}}^{\text{NN}}\} \approx \{\hat{\delta}_{t_k}, \dots, \hat{\delta}_{t_{k+N_p-1}}\}, \quad (10)$$

where $\delta_{t_k}^{\text{NN}} = (\delta_{1,t_k}^{\text{NN}}, \dots, \delta_{N_{\text{dof}}^{\text{lofi}},t_k}^{\text{NN}})$ denotes the component-wise output of the RNN. As numerous time steps are mapped simultaneously, the in- and output dimension of the RNN is $\mathbb{R}^{N_{\text{dof}}^{\text{lofi}} \times N_p}$. Calculating (10) with inputs $\{\hat{\mathbf{x}}_{t_k}\}_{k=l:N_p}^{(l+1)N_p-1}$ for $l = 0, 1, \dots, \frac{N_T^{\text{lofi}}}{N_p} - 1$ yields an approximation of $\hat{\delta}_{i,t_k}$ on the whole trajectory. Choosing a similar basis representation as in (9), we can define the RNN/FE hybrid model as

$$\delta_\theta(\mathbf{r}) = \sum_{i=1}^{N_{\text{dof}}^{\text{lofi}}} \delta_{i,t_k}^{\text{NN}} \phi_i(\mathbf{r}), \quad \forall k = 1, \dots, N_T^{\text{lofi}}. \quad (11)$$

As the FE basis functions already provide a basis for the discretized spatial domain, the RNN needs only to handle the variation of the coefficients in

time, thus significantly simplifying the optimization problem and reducing training times. In Figure 1, the vectors \mathbf{c}_t and \mathbf{h}_t , $t = t_k, \dots, t_{k+N_p-1}$, denote the cell state and hidden state of the LSTM cell. The cell state of the LSTM consists of a parameter vector controlling the gating mechanism of the LSTM cell and, ultimately, information flow, while the hidden state of the LSTM consists of the cell output, which is simultaneously fed to the consecutive cell and to the output layer. We choose rectified linear units (ReLU) activation functions, which is a necessary choice for the approximation of the piecewise and non-differentiable behavior occurring in phase transitions.

3.2. Normalization by non-dimensionalization

A significant drawback of NNs is their inability to adequately represent data with small values, a scenario which comes up when considering error functions. Thus, normalization procedures are in order, which scale the input data and significantly improve the performance of NNs. Especially in physical systems, the quantities of interest can become very small as they are expressed relative to very small physical constants. Examples of such constants are the magnetic permeability $\mu \sim 10^{-7} \frac{\text{Vs}}{\text{Am}}$ or the thermal conductivity $\kappa \sim 10^{-3} \frac{\text{W}}{\text{mK}}$. Small physical geometries induce similar problems. The resulting error functions of such systems consist of small, fluctuating values, thus requiring a normalization procedure which scales the dynamical system appropriately, while remaining physically conforming at the same time.

An example of such a scaling procedure is the non-dimensionalization of the physical system. In essence, non-dimensionalization removes the physical dimensions from underlying differential equations by suitable variable substitutions. The resulting differential equations have their physical dimensions partially or even completely removed. As an illustrative example, we present how the temporal and spatial differential operators transform under change of variables. Let $\mathbf{r} = (r_x, r_y)$ and $\tau = t_c^{-1}t$, $\underline{r}_x = r_{x,c}^{-1}r_x$, $\underline{r}_y = r_{y,c}^{-1}r_y$ for $t_c [\text{s}]$, $r_{x,c} [\text{m}]$, $r_{y,c}^{-1} [\text{m}] \in \mathbb{R}$, be a coordinate transformation for which physical dimensions have been removed. The non-dimensionalised n -th time derivative as well as the Laplace operator transformation is given by

$$\frac{\partial^n}{\partial t^n} = \frac{1}{t_c^n} \frac{\partial^n}{\partial \tau^n} \quad \text{and} \quad \Delta = \frac{1}{\sqrt{|g|}} \sum_{i=1}^2 \partial_i \left(\sqrt{|g|} g_{ii} \partial_i \right), \text{ with } g = \begin{pmatrix} r_{x,c}^{-2} & 0 \\ 0 & r_{y,c}^{-2} \end{pmatrix}, \quad (12)$$

where g is the metric tensor and Δ the Laplace-Beltrami operator. The transformed wave equation then reads

$$\left[\frac{1}{t_c^2} \frac{\partial^2}{\partial \tau^2} + c \left(\frac{1}{r_{x,c}^2} \frac{\partial^2}{\partial \underline{r}_x^2} + \frac{1}{r_{y,c}^2} \frac{\partial^2}{\partial \underline{r}_y^2} \right) \right] u(\tau, \underline{r}_x, \underline{r}_y) = f(\tau, \underline{r}_x, \underline{r}_y), \quad (13)$$

where the solution to the original system can then be recovered by the backwards transformation $t = t_c^{-1}\tau$, $r_x = r_{x,c}^{-1}\underline{r}_x$ and $r_y = r_{y,c}^{-1}\underline{r}_y$. The resulting system can then be scaled such that NNs can optimally fit the data, as well as conform to the physical equations.

3.3. Hybrid model training

In this section, we discuss the training of the RNN, including details on the choice of training data and how we deal with data sparsity. The training data set consists of snapshot data of the discrepancy function, which are calculated from the down-projected high-fidelity solution and the low-fidelity solution. Assuming N_T^{hifi} trajectory samples of the high-fidelity solution $\{\mathbf{x}_{t_k}^{\text{hifi}}\}_{t_k \leq N_T^{\text{hifi}}}$, we denote with $T_{\text{hifi}} := \{t_0, t_1, \dots, t_{N_T^{\text{hifi}}}\}$ the respective time instances on which they are defined. Then, we can partition the time axis of the BVP into separate intervals $I_k := [t_k, t_{k+1}]$ such that $[0, T] = \bigcup_{k=0}^{N_T^{\text{hifi}}} I_k$ holds for $t_0 = 0$ and $t_{N_T^{\text{hifi}}} = T$. As we can evaluate the low-fidelity model at more time instances than those included in the high-fidelity data, low-fidelity states $\mathbf{x}_{t_k}^{\text{lofi}}$ can be evaluated for $t_k \in T_{\text{hifi}}$, but also on intermediate time instances $t_k < t_{k_j} < t_{k+1}$ with $j = 1, \dots, N_{I_k}$, where N_{I_k} denotes the number of intermediate time steps in the interval I_k . Consequently, the low-fidelity states $\mathbf{x}_{t_k}^{\text{lofi}}$ are defined on more time steps, namely $T_{\text{lofi}} := T_{\text{hifi}} \cup \left\{ \bigcup_{k=1}^{N_T^{\text{hifi}}} \bigcup_{j=1}^{N_{I_k}} t_{k_j} \right\}$. We construct T_{lofi} by choice of the low-fidelity model, such that $|T_{\text{hifi}}| \leq |T_{\text{lofi}}|$ holds and the time instances are uniform, i.e., $t_{k+1} - t_k = \Delta t$, $\forall t_k, t_{k+1} \in T_{\text{lofi}}$. Especially the latter point is important for the inputs of RNNs. For a visualization of the difference between the sets T_{hifi} and T_{lofi} , see Figure 3.3. Given these considerations, the training data consisting of discrepancy function snapshots is given as the set

$$\mathcal{D}_{\text{d}} := \left\{ \mathcal{T}(\mathbf{x}_{t_k}^{\text{hifi}}) - \mathbf{x}_{t_k}^{\text{lofi}} \right\}_{t_k \in T_{\text{hifi}}}, \quad (14)$$

where \mathcal{T} is a linear projection operator and $t_k \in T_{\text{hifi}}$. Note that the sampled instances of the high-fidelity data are not chosen randomly. Instead, they depend on the dynamics of the underlying physical system. In areas where

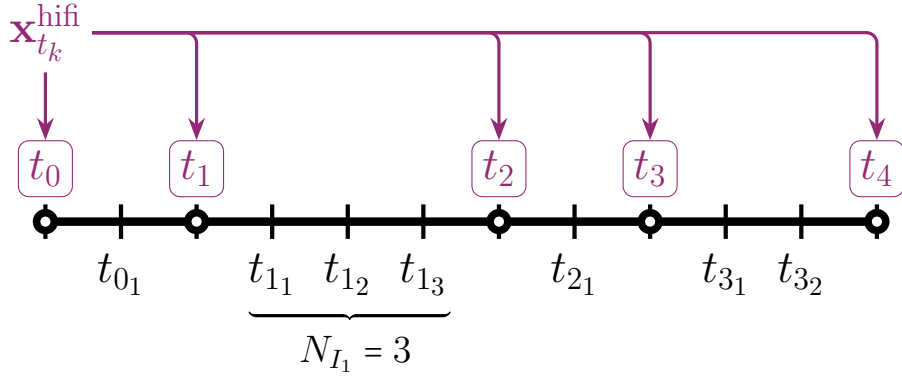


Figure 2: The high-fidelity solution $\mathbf{x}_{t_k}^{\text{hifi}}$ is defined on T_{hifi} . The intermediary time steps of the low-fidelity model are on the time axis. $N_{I_1} = 3$ denotes the number of intermediary steps for the interval I_1 .

the high-fidelity systems is very dynamic, for instance, when it is heavily excited, the trajectory is sampled more frequently than in areas where the system approaches steady state. In this work, we sample heuristically and note that there are more sophisticated methods to perform the data sampling, for instance, using active learning or optimal experimental design techniques.

Whilst sparse data sets are the norm for most practical scenarios, for example in measurement setups, NNs typically show bad interpolation behavior when trained solely with sparse data sets. This is partially due to the fact that no knowledge of the objective function is provided in sparsely sampled areas, wherein the RNN’s interpolation accuracy decreases dramatically. In these scenarios, one has to “inform” the NN on the correct mode of behavior. One way to achieve this would be to add physically motivated constraints to the loss function, an approach frequently pursued in so-called physics-informed machine learning [29]. Another approach is to upsample the available training data as to reflect correct physical behavior, an approach commonly used in game design and image processing [26, 31, 51]. The main difference between these two approaches is on how the information regarding the correct interpolation behavior is encoded. In the former case, it is encoded in the formulation of the optimization problem. In the latter case, in the artificial (upsampled) data points the model is trained with. The latter approach is explained in more detail in the next section.

3.4. Localized data upsampling and noise stabilization

In this work, we resort to the approach of data upsampling, such that model training is performed within a standard supervised learning context. Introducing physics-inspired loss functions, whilst also a promising avenue, has the drawback of significantly complicating the optimization problem, often resulting in elongated training times.

We propose an upsampling scheme based on a combination of localized, linear interpolation to calculate intermediate artificial system states for $t_k \in T_{\text{up}} := T_{\text{hifi}} \setminus T_{\text{lofi}}$, and a Gaussian prior for noise stabilization to prevent the overfitting phenomenon. Noise stabilization is a common approach in Gaussian Processes to improve numerical stability [4, 65] and can be used to prevent NNs from overfitting. The linear interpolation aspects controls the NN's behavior in the sparse data regime, whereas the prior distribution prevents the NN from overfitting. In each training epoch, the prior distribution is sampled to generate new artificial states that are locally bounded by the variance of the Gaussian prior. We choose a linear interpolation approach due to its simplicity and ease of use, as well as its applicability to a large category of problem types. We denote the locally linear interpolation function $\bar{\delta}_{I_k} : I_k \rightarrow \mathbb{R}^{N_{\text{dof}}^{\text{lofi}}}$ as

$$\bar{\delta}_{I_k}(t) = \frac{\delta_{t_k} t_{k+1} - \delta_{t_{k+1}} t_k}{t_{k+1} - t_k} + t \left(\frac{\delta_{t_{k+1}} - \delta_{t_k}}{t_{k+1} - t_k} \right). \quad (15)$$

Essentially, (15) interpolates linearly in intervals of sparse data, based on the boundary values found in the training data. We apply noise stabilization by assuming a Gaussian prior on the artificial intermediate states. Let $\bar{\delta}_{i,t_{k_j}} = \bar{\delta}_{I_k}(t_{k_j})|_{I_k}$ be evaluated in $t_{k_j} \in I_k$ for $j = 1, \dots, N_{I_k}$ and restricted to the i -th spatial dof. Then, we define the Gaussian prior

$$p(\bar{\delta}_{i,t_{k_j}}) = \bar{\delta}_{i,t_{k_j}} + \mathcal{N}\left(0, \alpha \left\| \bar{\delta}_{i,t_{k_j}} \right\|_2\right), \quad (16)$$

for $i = 1, \dots, N_{\text{dof}}^{\text{lofi}}$ and $t_{k_j} \in T_{\text{up}}$, where $\alpha \in \mathbb{R}$ is a weighting factor controlling the variance. The distribution (16) is defined locally for the individual dof, where a lower variance is assumed for dof close to zero, thus preserving known boundary conditions, and a larger variance is allowed in domains where the discrepancy is non-zero. An upsampled data set \mathcal{D}_{up} for $t_{k_j} \in T_{\text{up}}$ based on (16) is then given as

$$\mathcal{D}_{\text{up}} := \left\{ \delta_{t_{k_j}} \in \mathbb{R}^{N_{\text{dof}}^{\text{lofi}}} \mid \delta_{i,t_{k_j}} \sim p(\bar{\delta}_{i,t_{k_j}}), \quad i = 1, \dots, N_{\text{dof}}^{\text{lofi}} \right\}_{t_{k_j} \in T_{\text{up}}}. \quad (17)$$

In each training epoch of the RNN, \mathcal{D}_{up} is generated by sampling (16) for all spatial dof. Thus, the sparse time series is upsampled to a complete trajectory using the varying artificial system states in \mathcal{D}_{up} and the elements of \mathcal{D}_{d} which remain fixed as part of the ground truth.

The training of the RNN is based on a locally weighted loss function, given by

$$\mathcal{J}_{\theta} = \frac{1}{N_{\text{dof}}^{\text{lof}}} \left(\overbrace{\sum_{t_k \in T_{\text{hifi}}} \beta_{t_k} |\boldsymbol{\delta}_{t_k} - \boldsymbol{\delta}_{t_k}^{\text{NN}}|}^{\text{ground truth}} + \overbrace{\sum_{t_{k_j} \in T_{\text{up}}} |\boldsymbol{\delta}_{t_{k_j}}^* - \boldsymbol{\delta}_{t_{k_j}}^{\text{NN}}|}^{\text{artificial states}} \right), \quad (18)$$

where $\boldsymbol{\delta}_{t_k} \in \mathcal{D}_{\text{d}}$ are part of the ground truth states, $\boldsymbol{\delta}_{t_{k_j}}^* \in \mathcal{D}_{\text{up}}$ the sampled artificial states, $\beta_{t_k} \in \mathbb{R}$ a local, time-dependent weighting factors, and $|\cdot|$ the Euclidean norm. In the initial training stages, we choose $\beta_{t_k} = 1, \forall t_k \in T_{\text{hifi}}$, until the RNN has a coarse fit on the data. In the later training stages, we change the local weighting factors on \mathcal{D}_{d} to $\beta_{t_k} = 1 + \|\boldsymbol{\delta}_{t_k} - \boldsymbol{\delta}_{\theta}\|_2$, which are calculated by numerical quadrature. Note that $\beta_{t_k} \geq 1$. In that way, we ensure that the data set \mathcal{D}_{d} is always weighted more heavily than \mathcal{D}_{up} during RNN training. For the optimization, we use the adaptive moment estimation (ADAM) algorithm with learning rate decay.

4. Numerical Examples

In the following numerical investigations, we employ the proposed hybrid model to approximate discrepancy functions in three engineering test cases governed by transient PDEs, namely, heat diffusion on a heat sink, eddy-currents in a quadrupole magnet, and sound wave propagation inside a cavity. For each test case, we consider a high-fidelity and a low-fidelity FE representation of the BVP. The difference between the two lies in the FE mesh refinement, as well as in modeling errors in the material laws, excitation, and domain geometry, depending on the test case. To highlight the necessity of the upsampling approach proposed in Section 3.4, we consider hybrid models with and without data upsampling and observe the impact of overfitting in the latter case. Both simulations are then compared to reference data of the discrepancy function, which is calculated from densely sampled high-fidelity data. The trained hybrid models are then employed for bias correction of the low-fidelity models using (5), leading to significantly more accurate results. To assess the accuracy of the discrepancy function

approximation and the bias corrected model, we consider the relative $L^2(\Omega)$ errors

$$\Delta_{L^2} \delta_\theta := \frac{\int_{[0,T]} \|\delta_\theta - \delta_t\|_2 dt}{\int_{[0,T]} \|\delta_t\|_2 dt} \quad \text{and} \quad \Delta_{L^2} \mathbf{x} := \frac{\int_{[0,T]} \|\mathbf{x}_t - \mathcal{T}(\mathbf{x}_t^{\text{hifi}})\|_2 dt}{\int_{[0,T]} \|\mathcal{T}(\mathbf{x}_t^{\text{hifi}})\|_2 dt}, \quad (19)$$

where the $\|\cdot\|_2$ is approximated via numerical integration over the computational mesh and $\int_{[0,T]} \cdot dt$ via Riemannian sums. Last, considering the FE simulations, we restrict ourselves to the 2D case without loss of generality. Consequently, we can restrict our space of test functions to

$$H_0(\text{grad}; \Omega) := \{u \in L^2(\Omega) \text{ with } \nabla(u) \in L^2(\Omega) \text{ and } u|_{\partial\Omega} = 0\}, \quad (20)$$

for the derivation of the FE formulation in all test cases. Thus, $w \in H_0(\text{grad}; \Omega)$ are defined by the mesh nodes of the triangulation of Ω . For all test cases, we choose first order shape functions. For the FE implementation we use `gmsh` [20] and `FEniCSx` [2, 39, 57, 58]. RNNs are implemented using `jax/flax` [6, 24].

4.1. Heat diffusion on a heat sink

As first test case, we consider the heat diffusion problem on a 2D cross-section of a heat sink, see Figure 4.1 (left). The heat sink geometry is defined on the domain $\Omega = [-l, l]^2$, $l \in \mathbb{R}$, which consists of a thermally conductive region Ω_{con} and a less thermally conductive air region Ω_{air} . The boundary of the geometry consists of $\partial\Omega_d = \partial\Omega \cap \partial\Omega_{\text{air}}$, to which we apply homogeneous Dirichlet boundary conditions and $\partial\Omega_{nd} = \partial\Omega \cap \partial\Omega_{\text{con}}$, to which we apply non-homogeneous Dirichlet boundary conditions. The BVP reads

$$\begin{aligned} \rho c_v \frac{\partial u}{\partial t} - \nabla \cdot (\kappa \nabla u) &= 0 \text{ on } \Omega, \\ u|_{\partial\Omega_{nd}} &= c, \\ u|_{\partial\Omega_d} &= 0, \end{aligned} \quad (21)$$

where u is the temperature, ρc_v the heat capacity, κ the thermal conductivity, and c a fixed temperature. The non-homogeneous Dirichlet boundary condition signifies a heat source underneath the heat sink, while the homogeneous Dirichlet boundary conditions assume constant temperature on the boundary. On the fins of the heat sink, we assume a heat conductivity of $\kappa = 50 \text{ W (mK)}^{-1}$, following a linear deterioration of the heat conductivity by

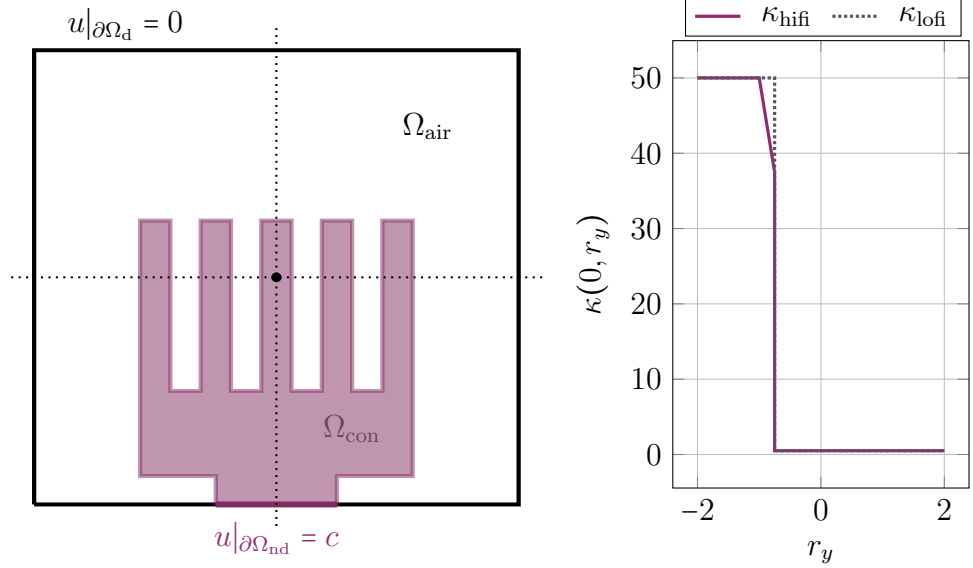


Figure 3: **Left:** Schematic of a heat sink cross-section, where Ω_{con} is the thermally conductive domain and Ω_{air} the non-conductive domain. Non-homogeneous Dirichlet boundary condition are applied at the heat sink base at $\partial\Omega_{\text{nd}} = \partial\Omega \cap \partial\Omega_{\text{con}}$. **Right:** Plot of the thermal conductivity of the material along the middle fin, where κ_{hifi} is the conductivity with defects and κ_{lofi} without. The conductivity in Ω_{air} is $\kappa = 0.5 \text{ W} (\text{mK})^{-1}$ for both cases.

25% close to the proximity of the tips. This deterioration can be attributed to material aging or other defects. Figure 4.1 (right) shows the thermal conductivity including material defects, κ_{hifi} , plotted against the thermal conductivity without material defects, κ_{lofi} , along the middle fin of the heat sink. In Ω_{air} we assume $\kappa = 0.5 \text{ W} (\text{mK})^{-1}$.

To solve the heat diffusion problem using the FE method, we introduce the corresponding variational form by multiplying (21) with a test function $w_i \in H_0(\text{grad}; \Omega)$ and integrate over the domain. The variational form reads

$$\int_{\Omega} \rho c_v \frac{\partial u}{\partial t} w_i \, d\Omega - \int_{\Omega} \nabla \cdot (\kappa \nabla u) w_i \, d\Omega = 0, \quad (22)$$

for $i = 1, \dots, N_{\text{dof}}^{\text{lofi}}$. Applying integration by parts and first order difference quotients $\frac{\partial u}{\partial t} = \frac{u_{t_{k+1}} - u_{t_k}}{\Delta t}$ results in the implicit Euler time stepping scheme

$$\int_{\Omega} \rho c_v u_{t_{k+1}} w_i \, d\Omega + \Delta t \int_{\Omega} \kappa \nabla u_{t_{k+1}} \cdot \nabla w_i \, d\Omega = \int_{\Omega} \rho c_v u_{t_k} w_i \, d\Omega. \quad (23)$$

We discretize the temperature $u = \sum_{j=1}^{N_{\text{dof}}^{\text{lofi}} + N_{\text{bdry}}^{\text{lofi}}} \hat{u}_j w_j$. The first $N_{\text{dof}}^{\text{lofi}}$ shape functions $w_j \in H_0(\text{grad}; \Omega)$ for $j = 1, \dots, N_{\text{dof}}^{\text{lofi}}$ are the trial functions and equal to the test functions, adopting the Ritz-Galerkin approach. $\{\hat{u}_j\}_{j=1}^{N_{\text{dof}}^{\text{lofi}}}$ are the dof. The additional $N_{\text{bdry}}^{\text{lofi}}$ shape functions w_j for $j = N_{\text{dof}}^{\text{lofi}} + 1, \dots, N_{\text{dof}}^{\text{lofi}} + N_{\text{bdry}}^{\text{lofi}}$ together with the coefficients $\{\hat{u}_j\}_{j=N_{\text{dof}}^{\text{lofi}}+1}^{N_{\text{dof}}^{\text{lofi}} + N_{\text{bdry}}^{\text{lofi}}}$ discretize the non-homogeneous Dirichlet data. The resulting system reads

$$(\Delta t \mathbf{A} + \mathbf{M}) \hat{\mathbf{u}}_{t_{k+1}} = \mathbf{M} \hat{\mathbf{u}}_{t_k}, \quad (24)$$

where \mathbf{A} is the stiffness matrix and \mathbf{M} the mass matrix and the individual entries of the respective matrices are given as

$$\mathbf{M}_{ij} = \int_{\Omega} \rho c_v w_i w_j \, d\Omega \quad \text{and} \quad \mathbf{A}_{ij} = \int_{\Omega} \kappa \nabla w_i \cdot \nabla w_j \, d\Omega. \quad (25)$$

The columns of \mathbf{A} and \mathbf{M} for $j = N_{\text{dof}}^{\text{lofi}} + 1, \dots, N_{\text{dof}}^{\text{lofi}} + N_{\text{bdry}}^{\text{lofi}}$ are shifted from the left to right-hand side of (27) by applying a Dirichlet lift [52].

For the simulation with either model, i.e, low- or high-fidelity, we assume $\rho c_v = 1 \text{ JK}^{-1} \text{m}^{-3}$, $c = 10 \text{ K}$, $\Delta t = 2 \cdot 10^{-2} \text{ s}$, and $N_T = 100$. The low-fidelity model $\Psi_{\text{lofi}}(\hat{\mathbf{u}}_{t_k}^{\text{lofi}} | \kappa_{\text{lofi}})$ has thermal conductivity κ_{lofi} with $N_{\text{dof}}^{\text{lofi}} = 278$, while the high-fidelity model $\Psi_{\text{hifi}}(\hat{\mathbf{u}}_{t_k}^{\text{hifi}} | \kappa_{\text{hifi}})$ has thermal conductivity κ_{hifi} and $N_{\text{dof}}^{\text{hifi}} = 1408$. The different material choices and mesh discretizations induce modeling and discretization errors between low-fidelity and high-fidelity model. A visualization of the heat distribution of the high-fidelity and low-fidelity model is depicted in Figure 5 (rows 1 and 3). In both cases, we can observe that the heat sink rapidly transports heat from the excited base to its surroundings, eventually reaching a steady-state.

To approximate the discrepancy function, we employ 19 out of 100 trajectory samples as training data, where more samples are chosen in the initial stages of excitation and a reduced number of samples when the system reaches steady-state. The training data instances are depicted as crosses at the respective time steps in Figure 4. We train the RNN according to the parameters in Table 2, from which we observe that 1000 training epochs are required to reduce $\Delta_{L^2} \delta_\theta$ of the upsampled model to 0.27% and equivalently, the non-upsampled model to 8.187%.

In Figure 4 we display the spatially integrated discrepancy function $\|\delta_t\|_2$ in each time step, once for the hybrid model, with and without upsampling, and once for reference data. In case the hybrid model is trained solely on the

sparse data set, we observe a good agreement on the training data, however, large errors appear for previously unseen data, due to overfitting. This phenomenon is especially pronounced in areas where there exist larger gaps in the training data, for example between the time steps $t_{30} = 0.6$ s and $t_{100} = 2$ s. However, we also note that upsampling is not necessary in all regions on the trajectory for the hybrid model to exhibit correct interpolation behavior, as can be observed between time steps $t_5 = 0.1$ s and $t_{15} = 0.3$ s for the non-upsampled model.

Description	Symbol	0-500	500-1000
Learning rate	η	$1 \cdot 10^{-3}$	$1 \cdot 10^{-4}$
Local weighting factors	β	\times	\checkmark
Variance weighting factor	α	$\frac{1}{25}$	$\frac{1}{25}$
Error with upsampling	$\Delta_{L^2} \delta_{\theta^{\text{up}}}$	2.502 %	0.270 %
Error without upsampling	$\Delta_{L^2} \delta_{\theta}$	10.014 %	8.187 %

Table 1: Training parameters and hybrid model errors for the heat sink test case. The RNN has 278 neurons and considers $N_p = 2$ LSTM cells (consecutive time steps).

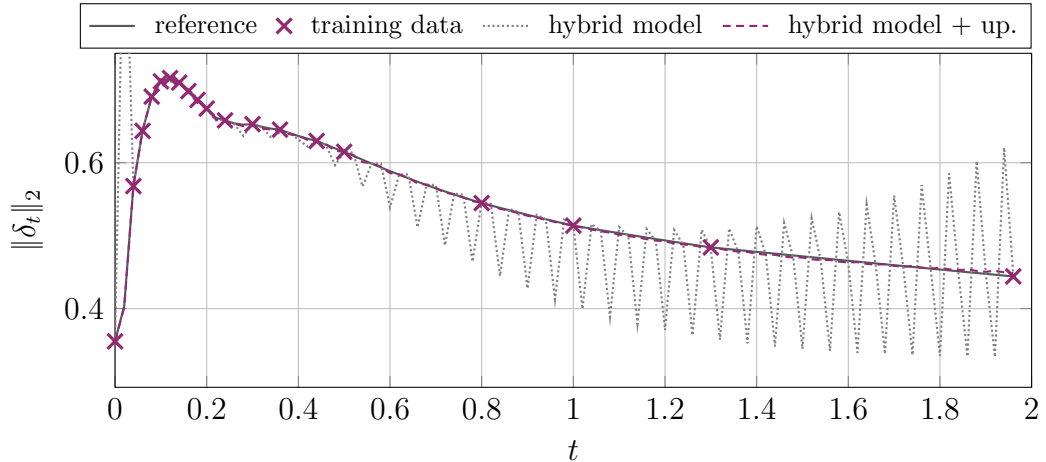


Figure 4: Spatially integrated discrepancy function $\|\delta_t\|_2$ for $t_0 = 0$ s until $t_{100} = 2$ s. The reference and the hybrid model with and without artificial upsampling are depicted. The training data is indicated at the respective time steps with \times .

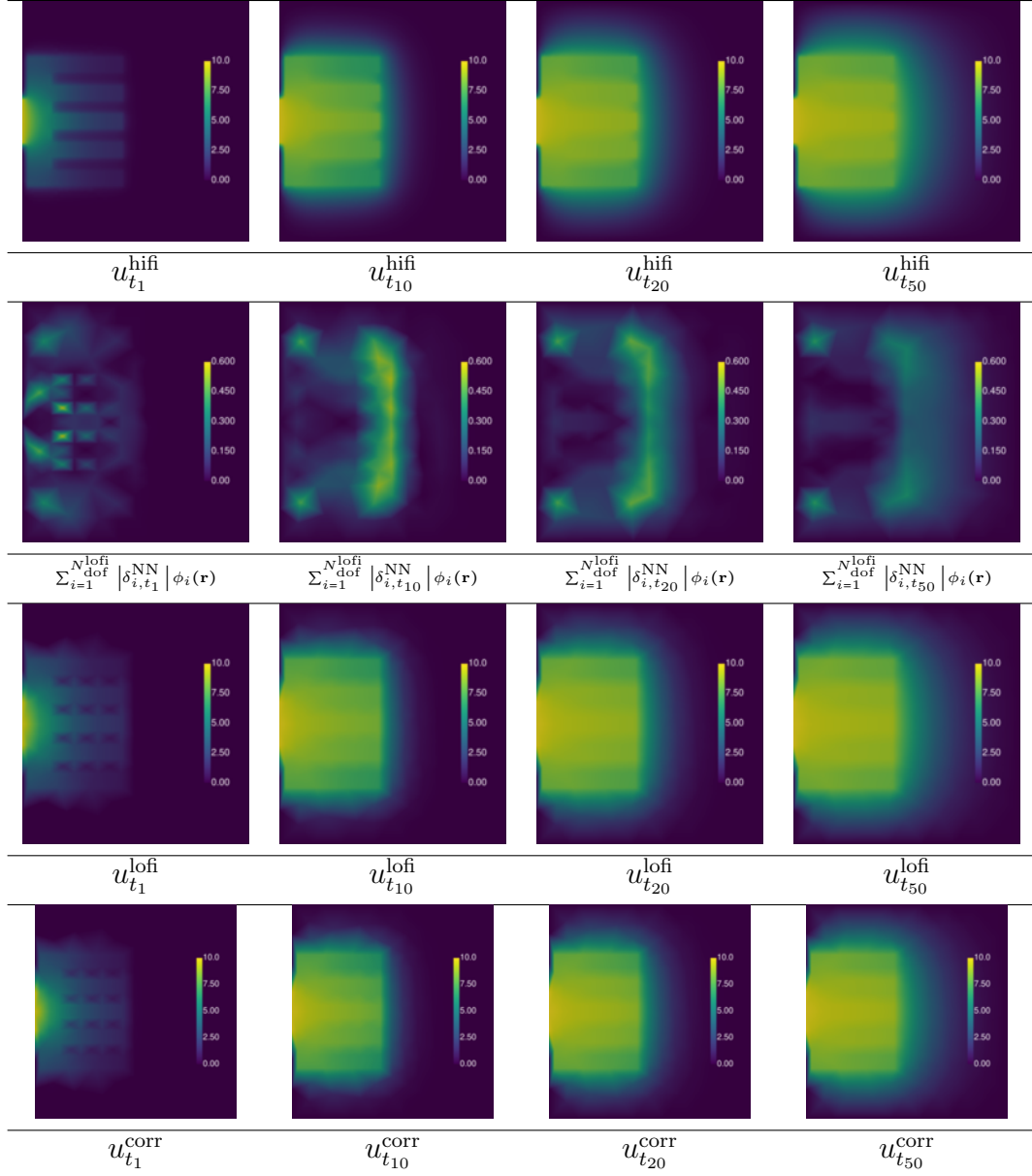


Figure 5: Transient heat diffusion for $k = 1, 10, 20, 50$.

Row 1: High-fidelity model, parametrized by κ_{hifi} .

Row 2: Absolute values of the discrepancy function coefficients.

Row 3: Low-fidelity model, parametrized by κ_{lofi} ($\Delta_{L^2} u^{\text{lofi}} = 2.73\%$).

Row 4: Bias corrected model ($\Delta_{L^2} u^{\text{corr}} = 7.59 \cdot 10^{-3}\%$).

In Figure 5 (row 2), we observe the absolute value of the discrepancy function between the low and high fidelity model. As expected, the maximum error is observed at the tips of the heat sink fins, that is, in the area where the material defect occurs. Figure 5 (row 4) shows the bias corrected model, for which we have $\Delta_{L^2} u^{\text{corr}} = 7.59 \cdot 10^{-3}\%$. Compared to $\Delta_{L^2} u^{\text{lofi}} = 2.73\%$, this is a significant correction to the low-fidelity model.

4.2. Transient eddy-current problem in a quadrupole magnet

As second test case, we examine the transient eddy-current problem on a 2D cross-section of a quadrupole magnet. The geometry is depicted in Figure 6 (left) [15]. The quadrupole is defined on a circular domain Ω , which consists of an iron yoke Ω_{Fe} , coils for current excitation Ω_s , and an aperture Ω_p . The domain boundary $\partial\Omega$ consists of the outer boundary of the iron domain $\partial\Omega_{\text{Fe}}$. The BVP describing the dynamical system is given by the magneto-quasistatic Maxwell equations. Choosing the vector potential ansatz $\mathbf{b} = \nabla \times \mathbf{a}$, where \mathbf{a} is the magnetic vector potential and \mathbf{b} the magnetic flux density, the eddy-current problem can be given as the time-dependent BVP

$$\begin{aligned} \nabla \times (\nu \nabla \times \mathbf{a}) + \sigma \frac{\partial \mathbf{a}}{\partial t} &= \mathbf{j}_s, \\ \mathbf{a}|_{\partial\Omega} &= 0, \end{aligned} \quad (26)$$

where \mathbf{j}_s the source current density. For the current excitation, we assume the current $I_{\text{hifi}}(t)$ depicted in Figure 6 (right). This choice of current excitation is motivated qualitatively by the ramping procedure that provides a linear field increase during acceleration with current plateaus for beam insertion and extraction and a current decay after switch-off. An approximate current density $I_{\text{lofi}}(t)$ is additionally considered, also depicted in Figure 6, which consists of a linear ramp and de-ramp. In both cases, the currents are distributed in the excitation domain, yielding a current density that can be calculated by $\mathbf{j}_s(\mathbf{r}, t) = |\Omega_s|^{-1} I(t) \mathbf{e}_z$, where \mathbf{e}_z is the unit vector in z -direction. To confine the magnetic quadrupole field inside the magnet, we choose homogeneous boundary conditions on $\partial\Omega$.

Similar to the previous section, we express (26) in its variational form and spatially discretize with vectorial first-order shape and test functions over a triangulation of Ω . Due to geometrical considerations, we can safely neglect transverse effects of the vector potential, which results in a single vectorial component $\mathbf{w}_i = w_i \mathbf{e}_z$, with $w_i \in H_0(\text{grad}; \Omega)$. The magnetic vector

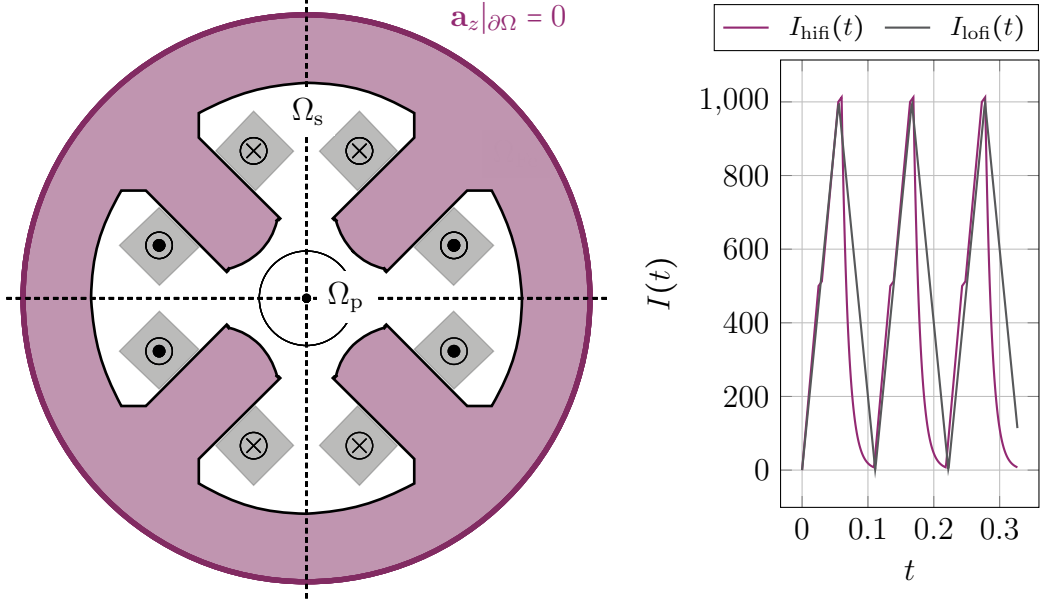


Figure 6: **Left:** Schematic of the quadrupole magnet, where Ω_{Fe} denotes the domain of the iron yoke, Ω_s the domain of current excitation and Ω_p the air domain. **Right:** Current excitation I_{hifi} for the high-fidelity model and I_{lofi} for the low-fidelity model.

potential is approximated via the ansatz function $\mathbf{a} = \sum_{j=1}^{N_{\text{dof}}^{\text{lofi}}} \hat{a}_j \mathbf{w}_j$, where the dof $\{\hat{a}_j\}_{j \leq N_{\text{dof}}^{\text{lofi}}}$ lie on the mesh nodes. In matrix-vector notation, the FE formulation reads

$$(\Delta t \mathbf{A} + \mathbf{M}) \hat{\mathbf{a}}_{t_{k+1}} = \Delta t \mathbf{b}(t_{k+1}) + \mathbf{M} \hat{\mathbf{a}}_{t_k}, \quad (27)$$

where \mathbf{A} and \mathbf{M} are the stiffness and mass matrix, respectively, and \mathbf{b} is the loading vector. The entries of \mathbf{A} and \mathbf{M} are given as

$$\mathbf{A}_{ij} = \int_{\Omega} (\nu \nabla \times \mathbf{w}_i) \cdot (\nabla \times \mathbf{w}_j) d\Omega \quad \text{and} \quad \mathbf{M}_{ij} = \int_{\Omega} \sigma \mathbf{w}_i \cdot \mathbf{w}_j d\Omega, \quad (28)$$

while the entries of the right hand side loading vector are

$$\mathbf{b}_i(t_k) = \int_{\Omega} \mathbf{j}_s(t_k) \cdot \mathbf{w}_i d\Omega. \quad (29)$$

For the simulation, we assume $\sigma_{\text{Fe}} = 1.04 \cdot 10^7 \text{ Sm}^{-1}$ and $\nu_{\text{Fe}} = 2 \cdot 10^{-3} \nu_0$ in Ω_{Fe} , and $\sigma = 1 \text{ Sm}^{-1}$ and $\nu = \nu_0$ in Ω_p and Ω_s . Furthermore, we assume a constant time step of $\Delta t = 1 \cdot 10^{-2} \text{ s}$ and $N_T = 327$ time steps.

The low-fidelity model $\Psi_{\text{lofi}}(\hat{\mathbf{a}}_{t_{k+1}}^{\text{lofi}}, \hat{\mathbf{a}}_{t_k}^{\text{lofi}}, \Delta t | I_{\text{lofi}}(t_{k+1}))$ is parametrized with the current I_{lofi} and mesh resolution $N_{\text{dof}}^{\text{lofi}} = 895$, while the high-fidelity model $\Psi_{\text{hifi}}(\hat{\mathbf{a}}_{t_{k+1}}^{\text{hifi}}, \hat{\mathbf{a}}_{t_k}^{\text{hifi}}, \Delta t | I_{\text{hifi}}(t_{k+1}))$ with current I_{hifi} and $N_{\text{dof}}^{\text{hifi}} = 277\,594$. Both multi-fidelity models are non-dimensionalized as described in Section 3.2, such that the magnetic vector potential is normalized to the unit square.

Description	Symbol	0-500	500-1000
Learning rate	η	$1 \cdot 10^{-3}$	$1 \cdot 10^{-4}$
Local weighting factors	β	\times	\checkmark
Variance weighting factor	α	$\frac{1}{25}$	$\frac{1}{25}$
Error with upsampling	$\Delta_{L^2} \delta_{\theta^{\text{up}}}$	2.806 %	1.538 %
Error without upsampling	$\Delta_{L^2} \delta_{\theta}$	13.094 %	8.187 %

Table 2: Training parameters and hybrid model errors for the quadrupole magnet test case. The RNN has 895 neurons and considers $N_p = 2$ LSTM cells (consecutive time steps).

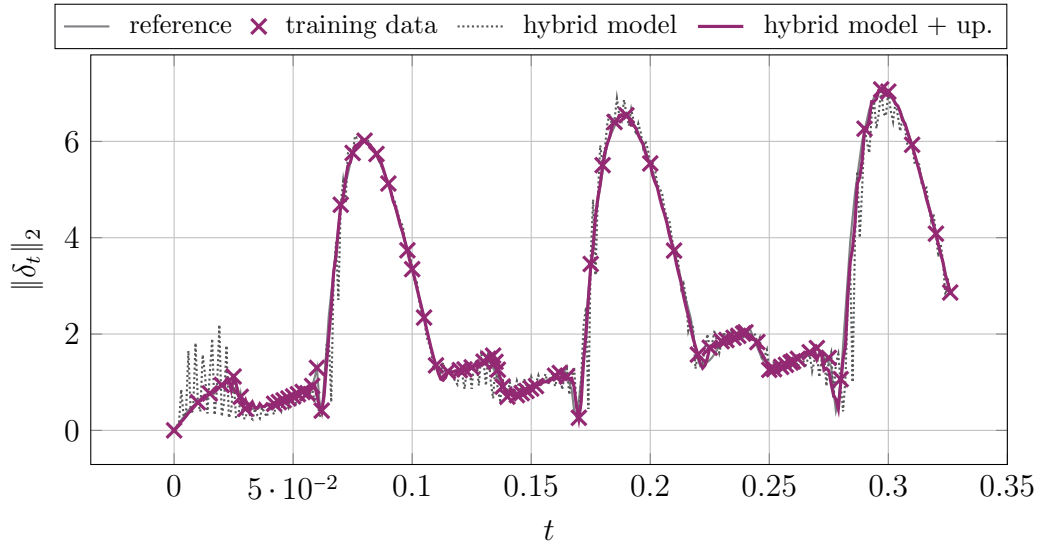


Figure 7: Spatially integrated discrepancy function $\|\delta_t\|_2$ for $t_0 = 0\text{s}$ until $t_{327} = 0.327\text{s}$. The reference and the hybrid model with and without artificial upsampling are depicted. The training data is indicated at the respective time steps with \times .

A visualization of the potential distribution of the high-fidelity and low-fidelity model is depicted in Figure 8 (rows 1 and 3). In both cases, we

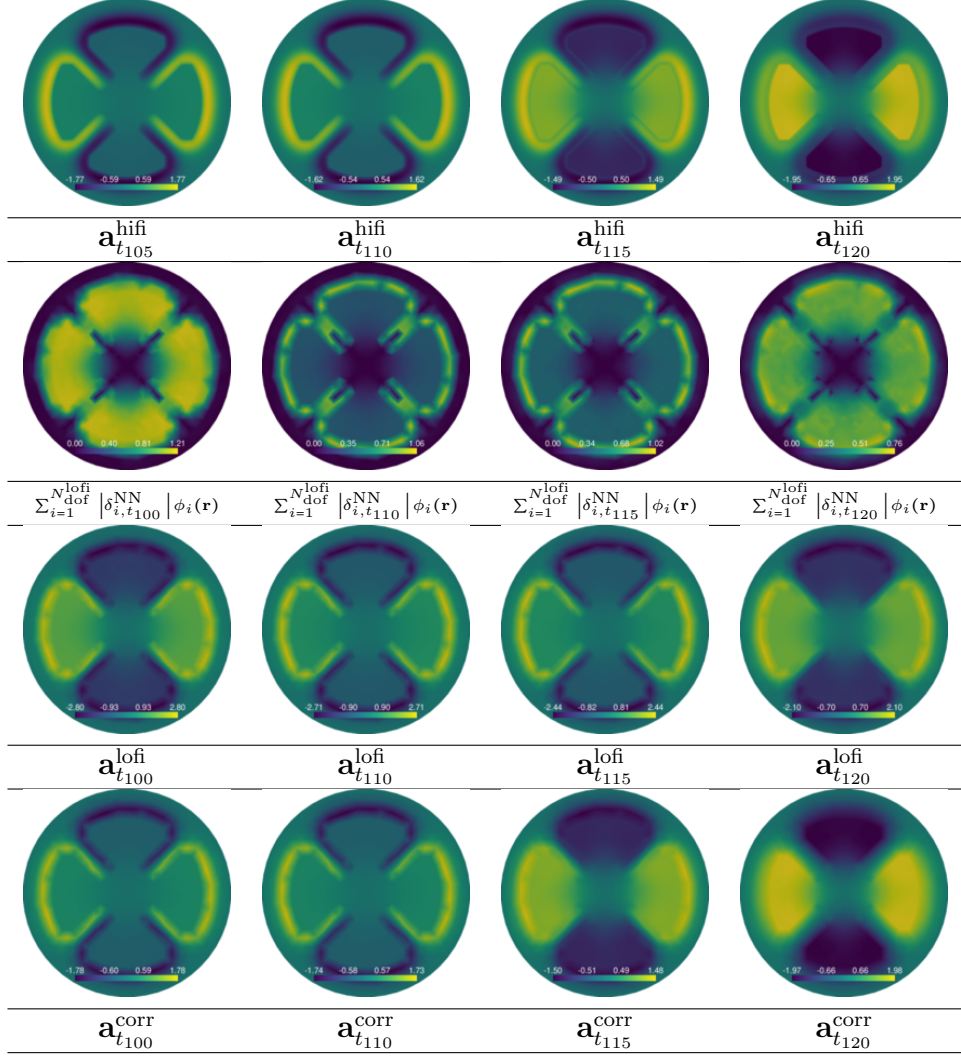


Figure 8: Transient eddy-current simulation for $k = 105, 110, 115, 120$.

Row 1: High-fidelity model, parametrized by $I_{\text{hifi}}(t)$.

Row 2: Absolute values of the discrepancy function coefficients.

Row 3: Low-fidelity model, parametrized by $I_{\text{lofi}}(t)$ ($\Delta_{L^2} \mathbf{a}^{\text{lofi}} = 39.847\%$).

Row 4: Bias corrected model ($\Delta_{L^2} \mathbf{a}^{\text{corr}} = 0.613\%$).

can observe the eddy current phenomenon occurring in the iron yoke $\partial\Omega_{\text{Fe}}$. As training data, we use 79 out of 327 trajectory samples at the respective time steps, depicted as crosses in Figure 7. In this test case, we increase the samples in areas where the current excitation changes from an increasing

to a decreasing flank. We train the model according to the parameters in Table 2, from which we observe that 1000 training epochs are required to reduce $\Delta_{L^2} \delta_\theta$ to 1.538% for the upsampled model, and to 8.187% for the non-upsampled model.

In Figure 7 we display the spatially integrated discrepancy function $\|\delta_t\|_2$ at each time step, for the hybrid model with and without upsampling and the reference data. If the hybrid model is trained using solely the sparse data set, we observe a good agreement on the data points. However, the model overfits and performs poorly for previously unseen data, albeit not as strongly as in the heat sink test case. This phenomenon is again prevalent in domains with sparse training data. Similar to the previous section, the hybrid model with artificial upsampling generally yields good agreement on the complete data set. However, there are certain areas in which the approximation is suboptimal, in particular when the current excitation changes from a rising to a falling flank.

A visualization of the discrepancy is given in Figure 8 (row 2), where we observe that the discrepancy primarily occurs at the interface between the iron and the air domain. In Figure 8 (row 4) shows the bias corrected model, for which we have $\Delta_{L^2} \mathbf{a}^{\text{corr}} = 0.613\%$. Compared to $\Delta_{L^2} \mathbf{a}^{\text{lofi}} = 39.847\%$, this is a significant correction to the low-fidelity model. The correction is obvious both visually and by comparing the approximation errors of the low-fidelity and the bias corrected models.

4.3. Wave propagation in a cavity

For the third test case, we consider wave propagation in a closed cavity, where one commonly aims at detecting resonance frequencies and eigenmodes. After excitation, the wave propagates through the cavity until it eventually dissipates and the dominant frequencies are identified. As to the geometry of the cavity, we assume a “true” geometry Ω_{hifi} , with rounded-off corners between the connectors and the cavity itself, as well as an approximate design, Ω_{lofi} , with sharp corners at the connectors. Both geometries are depicted in Figure 9 (left). The equation describing the BVP reads

$$\begin{aligned} \frac{\partial^2 u}{\partial t^2} - v^2 \Delta u &= f & (30) \\ u|_{\partial\Omega} &= 0, \end{aligned}$$

where u is the acoustic pressure field, v is the velocity of the propagating wave, $f \in \mathcal{C}^\infty(\Omega)$ the excitation function, and $\Omega \in \{\Omega_{\text{lofi}}, \Omega_{\text{hifi}}\}$ the low

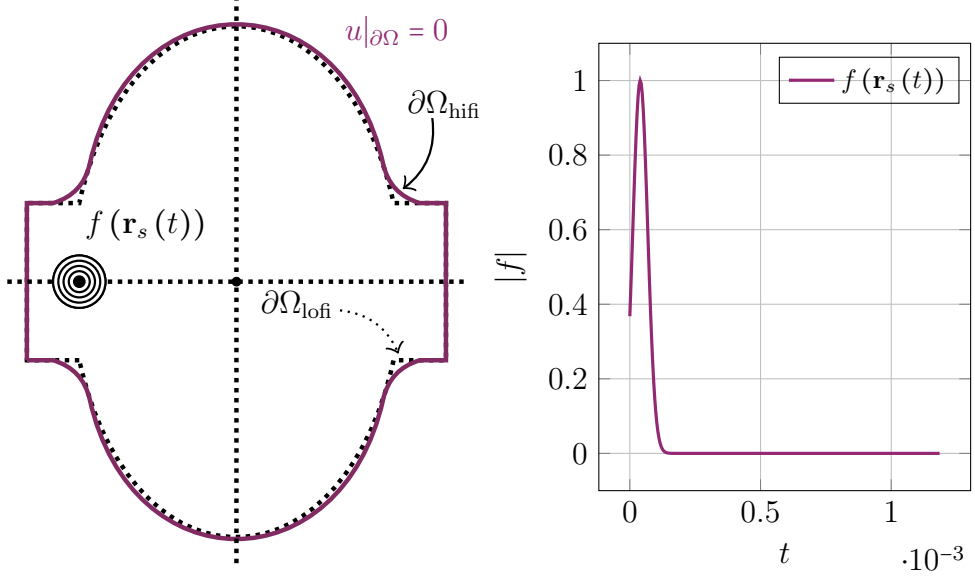


Figure 9: **Left:** Schematic of the cavity, where $\partial\Omega_{\text{hifi}}$ indicates the design with round corners (solid purple line) and $\partial\Omega_{\text{lofi}}$ the design with sharp corners (dotted black line). The point of excitation is indicated on the left of the cavity. **Right:** Excitation function $f(\mathbf{r}_s(t))$ over time.

and high-fidelity domains. For boundary conditions, we apply homogeneous Dirichlet boundary conditions on $\partial\Omega$, such that the wave is reflected off the cavity walls and contained therein. The wave excitation f is a Gaussian impulse, as shown in Figure 9 (right), applied as a point source at $\mathbf{r}_s \in \Omega$ as indicated in Figure 9 (left).

Similar to the previous sections, we express (30) in its variational form and spatially discretize with first-order shape and test functions $w_i \in H_0(\text{grad}; \Omega)$. The wave equation solution is approximated via $u = \sum_{j=1}^{N_{\text{dof}}^{\text{lofi}}} \hat{u}_j w_j$, where the dof $\{\hat{u}_j\}_{j \leq N_{\text{dof}}^{\text{lofi}}}$ lie on the mesh nodes. As (30) is an equation of second order, discretization in time requires a central differences scheme $\frac{\partial^2 u}{\partial t^2} = \frac{u_{t_{k+1}} - 2u_{t_k} + u_{t_{k-1}}}{\Delta t^2}$. The resulting discretized FE system reads

$$(\mathbf{M} + v^2 \Delta t^2 \mathbf{A}) \hat{\mathbf{u}}_{t_{k+1}} = \Delta t^2 \mathbf{b}(t_{k+1}) + 2 \mathbf{M} \hat{\mathbf{u}}_{t_k} - \mathbf{M} \hat{\mathbf{u}}_{t_{k-1}}, \quad (31)$$

where $\hat{\mathbf{u}}$ is a vector containing the dof of the FE basis and the mass and

stiffness matrices are given as

$$\mathbf{M}_{ij} = \int_{\Omega} w_i w_j d\Omega \quad \text{and} \quad \mathbf{A}_{ij} = \int_{\Omega} \nabla w_i \cdot \nabla w_j d\Omega, \quad (32)$$

and the right hand side loading vector \mathbf{b} is given at each time instance t_k as

$$\mathbf{b}_i(t_k) = \int_{\Omega} f(t_k) w_i d\Omega. \quad (33)$$

For the simulation, we assume $v = 343 \text{ ms}^{-1}$, $\Delta t = 4 \cdot 10^{-5} \text{ s}$, and $N_T = 100$ time steps. The low-fidelity model $\Psi_{\text{lofi}}(\hat{\mathbf{u}}_{t_{k+1}}^{\text{lofi}}, \hat{\mathbf{u}}_{t_k}^{\text{lofi}}, \hat{\mathbf{u}}_{t_{k-1}}^{\text{lofi}}, \Delta t | \Omega_{\text{lofi}})$ uses the approximate cavity geometry Ω_{lofi} with $N_{\text{dof}}^{\text{lofi}} = 169$. The high-fidelity model $\Psi_{\text{hifi}}(\hat{\mathbf{u}}_{t_{k+1}}^{\text{hifi}}, \hat{\mathbf{u}}_{t_k}^{\text{hifi}}, \hat{\mathbf{u}}_{t_{k-1}}^{\text{hifi}}, \Delta t | \Omega_{\text{hifi}})$ uses the “true” cavity geometry Ω_{hifi} with $N_{\text{dof}}^{\text{hifi}} = 3997$. The modeling and discretization errors are here induced by the geometry variation and the difference in mesh discretization. A visualization of the wave propagation of the high-fidelity and low-fidelity model is depicted in Figure 11 (rows 1 and 3). We observe that both waves propagate simultaneously, however, the low-fidelity solution is much coarser and its magnitude is significantly off.

For the discrepancy function approximation, we use 51 out of 100 trajectory instances as training data, depicted as crosses at the respective time steps in Figure 10. The hybrid model is trained according to the parameters in Table 3, from which we observe that 2500 training epochs are required to reduce $\Delta_{L^2} \delta_\theta$ to 0.200% for the upsampled model and to 14.797% for the non-upsampled model. In Figure 10, the spatially integrated discrepancy function $\|\delta_t\|_2$ is displayed at each time step, for the hybrid model with and without upsampling and the reference data. Similar to the previous sections, the hybrid model with artificial upsampling generally yields good agreement

Description	Symbol	0-1000	1000-2000	2000-2500
Learning rate	η	$1 \cdot 10^{-3}$	$5 \cdot 10^{-4}$	$1 \cdot 10^{-4}$
Local weighting factors	β	\times	\times	\checkmark
Variance weighting factor	α	$\frac{1}{100}$	$\frac{1}{100}$	$\frac{1}{100}$
Error with upsampling	$\Delta_{L^2} \delta_{\theta^{\text{up}}}$	2.587%	0.436%	0.200%
Error without upsampling	$\Delta_{L^2} \delta_\theta$	20.035%	17.195%	14.797%

Table 3: Training parameters and hybrid model errors for the waveguide test case. The RNN has 169 neurons and considers $N_p = 3$ LSTM cells (consecutive time steps).

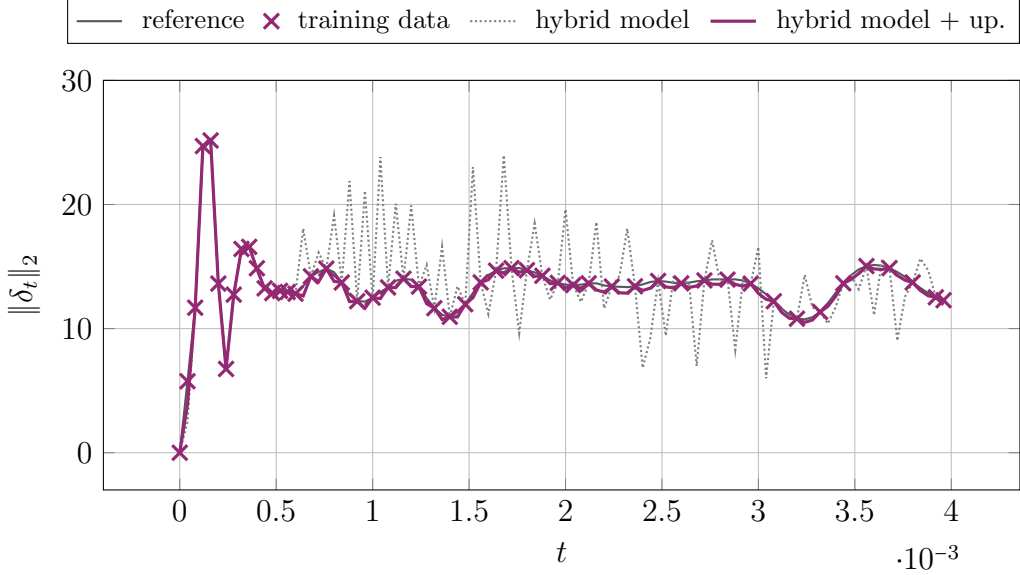


Figure 10: Spatially integrated discrepancy function $\|\delta_t\|_2$ for the time $t_0 = 0$ s until $t_{100} = 4 \cdot 10^{-3}$ s. The reference and the hybrid model with and without artificial upsampling scheme are depicted. The training data is indicated at the respective time steps with \times .

on the complete data set and the hybrid model without upsampling tends to overfit in regions with sparse data. Nevertheless, in this case, we require a larger training data set to achieve a good approximation, that is, slightly more than half of the available samples. This can be attributed to the fact that the underlying dynamical system is of second order and that the underlying discrepancy function exhibits locally non-smooth behavior. Consequently, higher demands are placed on the choice of linear upsampling scheme resulting in the training data to be sampled more densely.

A visualization of the discrepancy function is given in Figure 11 (row 2), where we observe in $t_{50} = 2 \cdot 10^{-3}$ s and $t_{60} = 2.4 \cdot 10^{-3}$ s that a significant portion of the error occurs near the variation in the geometry. In Figure 11 (row 4), the solution of the bias corrected model is shown, for which we have $\Delta_{L2} u^{\text{corr}} = 9.99 \cdot 10^{-2} \%$. In comparison to $\Delta_{L2} u^{\text{lofi}} = 27.53 \%$, we again verify that a significant correction to the low-fidelity model has been achieved.

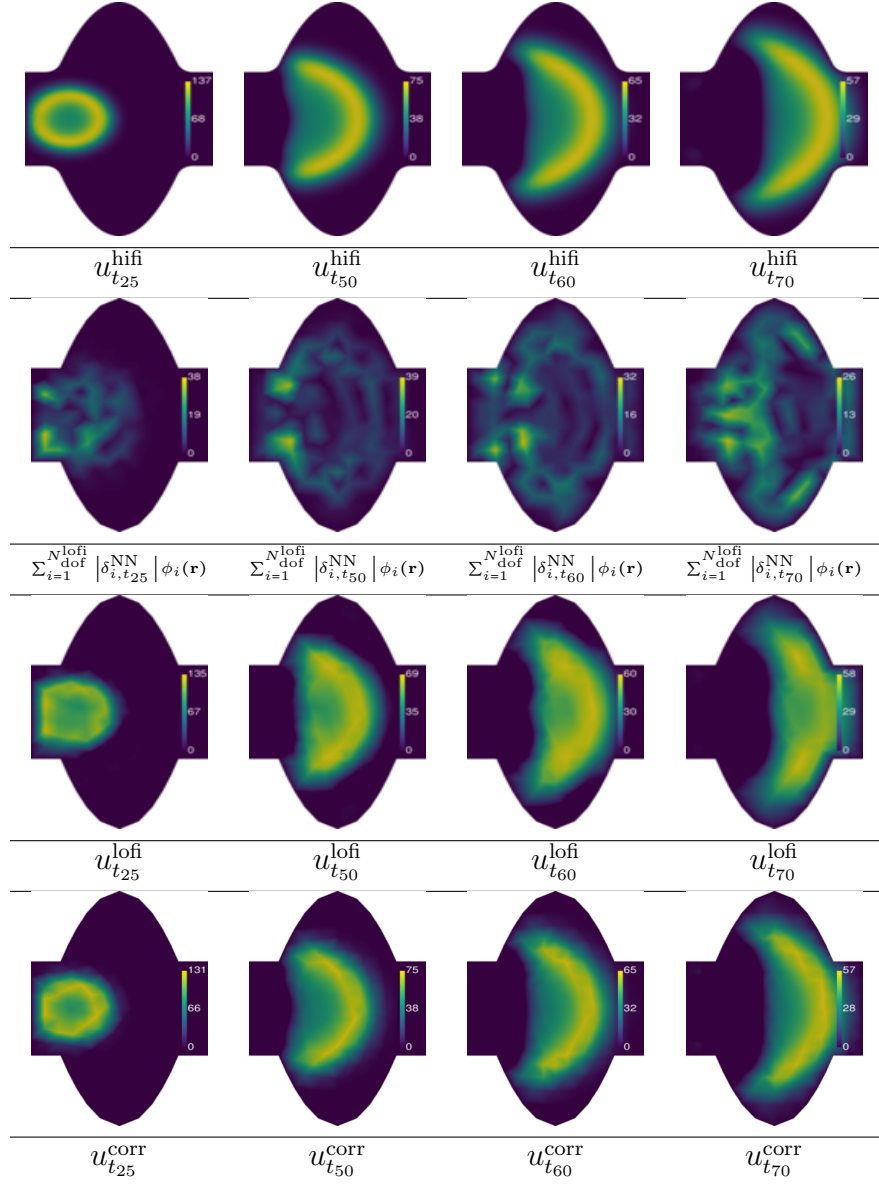


Figure 11: Wave propagation for $k = 25, 50, 60, 70$.

Row 1: High-fidelity model, parametrized by Ω_{hifi} .

Row 2: Absolute values of the discrepancy function coefficients.

Row 3: Low-fidelity model, parametrized by Ω_{lofi} . ($\Delta_{L^2} u^{\text{lofi}} = 27.53\%$).

Row 4: Bias corrected model ($\Delta_{L^2} u^{\text{corr}} = 9.99 \cdot 10^{-2}\%$).

5. Conclusion and Outlook

This work presented a hybrid modeling framework for the approximation and correction of model bias in the setting of multi-fidelity modeling and simulation of dynamic/transient systems. The proposed hybrid modeling approach combines standard FE approximation with an RNN, where the former accounts for the spatial effects of the approximation and latter for the temporal dynamics. The hybrid model first approximates the discrepancy between models of varying fidelity and is subsequently used to correct the low-fidelity models and increase their accuracy.

The presented numerical results show that the proposed hybrid modeling method is capable of yielding accurate approximations of the discrepancy function and, accordingly, significantly improved bias corrected models, for a variety of dynamical FE engineering simulations. In all considered test cases, the discrepancy function is approximated with an error below 2%, even if it displays a locally non-smooth behavior. Furthermore, the hybrid model remains accurate even if sparse training data sets are employed, given that a suitable upsampling scheme is provided, which controls the interpolation behavior in regions with only sparse data. Local weighting factors further ensure that the RNN provides a good fit of the training data and avoids over-smoothing.

In all considered test cases, the RNNs, consequently, the hybrid model is trained to sufficient accuracy after 1000 - 2500 epochs, thus resulting in quite modest training times, given the dimensionality of input and output. This is accomplished due to the nature of the proposed hybrid model, which splits spatial and temporal dependencies. The model already provides a spatial basis in form of the FE basis functions, hence, the RNN focuses on approximating the temporal dependencies only, which is a task very much suited to RNNs in general.

Despite the promising results shown in this work, there are limitations to the proposed hybrid modeling method worth mentioning. First, the accuracy of the hybrid model depends significantly on the upsampling scheme, especially within the domains with sparse data. The choice of upsampling scheme is thus problem dependent and requires assumptions on the underlying dynamical systems and discrepancy functions. In addition, the training data cannot be chosen completely at random, as samples within specific regions of the trajectory contain more information about the underlying dynamics than others. Introducing an optimal experimental design approach, e.g., knowing

a priori which time steps to sample as to achieve a good approximation, would be advisable. Finally, the projection operator is problem dependent as well, depending primarily on the choice of basis functions used to represent the discrepancy function. In the context of this work, this choice comes naturally due to the use of the FE method, however, the generalization to other basis representations should be explored.

To provide an outlook, there are numerous possible extensions to the presented methodology. Apart from considering more sophisticated RNN architectures, a possible avenue would be to explore localized Gaussian Processes with physics-inspired priors to upsample the physical data in a better way [23, 65]. Another possibility would be to include physics inspired loss functions, similar to the concept of PINNs [8, 29, 53], as a substitute or complement to data upsampling. Last, the performance of hybrid models trained with real-world observations, for example, collected from measurements or experiments, could be investigated. In such cases, one would face the additional task noise treatment, exemplarily, separating noise from the underlying trajectory data.

Acknowledgements

The authors would like to thank Armin Galetzka for thoroughly reading this manuscript and for providing helpful insights for improvements. Moritz von Tresckow acknowledges the support of the German Federal Ministry for Education and Research (BMBF) via the research contract 05K19RDB. Dimitrios Loukrezis and Herbert De Gersem acknowledge the support of the German Research Foundation (DFG) via the research grant TRR 361 (grant number: 492661287).

References

- [1] Mark Alber, Adrian Buganza Tepole, William R Cannon, Suvranu De, Salvador Dura-Bernal, Krishna Garikipati, George Karniadakis, William W Lytton, Paris Perdikaris, Linda Petzold, et al. Integrating machine learning and multiscale modeling—perspectives, challenges, and opportunities in the biological, biomedical, and behavioral sciences. *NPJ digital medicine*, 2(1):115, 2019.
- [2] M. S. Alnaes, A. Logg, K. B. Ølgaard, M. E. Rognes, and G. N. Wells. Unified form language: A domain-specific language for weak formula-

tions of partial differential equations. *ACM Transactions on Mathematical Software*, 40, 2014.

- [3] Paul D. Arendt, Daniel W. Apley, and Wei Chen. Quantification of Model Uncertainty: Calibration, Model Discrepancy, and Identifiability. *Journal of Mechanical Design*, 134(10), 09 2012. 100908.
- [4] J Bernardo, J Berger, APAFMS Dawid, A Smith, et al. Regression and classification using gaussian process priors. *Bayesian statistics*, 6:475, 1998.
- [5] Malte Braack and Alexandre Ern. A posteriori control of modeling errors and discretization errors. *Multiscale Modeling & Simulation*, 1(2):221–238, 2003.
- [6] James Bradbury, Roy Frostig, Peter Hawkins, Matthew James Johnson, Chris Leary, Dougal Maclaurin, George Necula, Adam Paszke, Jake VanderPlas, Skye Wanderman-Milne, and Qiao Zhang. JAX: composable transformations of Python+NumPy programs, 2018.
- [7] David Burg and Jesse H Ausubel. Moore’s law revisited through intel chip density. *PloS one*, 16(8):e0256245, 2021.
- [8] Shengze Cai, Zhiping Mao, Zhicheng Wang, Minglang Yin, and George Em Karniadakis. Physics-informed neural networks (pinns) for fluid mechanics: A review. *Acta Mechanica Sinica*, 37(12):1727–1738, 2021.
- [9] Giuseppe Carleo, Ignacio Cirac, Kyle Cranmer, Laurent Daudet, Maria Schuld, Naftali Tishby, Leslie Vogt-Maranto, and Lenka Zdeborová. Machine learning and the physical sciences. *Reviews of Modern Physics*, 91(4):045002, 2019.
- [10] Jie Chen, Yi Gao, and Yongming Liu. Multi-fidelity data aggregation using convolutional neural networks. *Computer Methods in Applied Mechanics and Engineering*, 391:114490, 2022.
- [11] Leiyu Chen, Shaobo Li, Qiang Bai, Jing Yang, Sanlong Jiang, and Yanning Miao. Review of image classification algorithms based on convolutional neural networks. *Remote Sensing*, 13(22):4712, 2021.

- [12] Wei Chen, Ying Xiong, Kwok-Leung Tsui, and Shuchun Wang. A design-driven validation approach using bayesian prediction models. 2008.
- [13] Paul B Conn, Devin S Johnson, Perry J Williams, Sharon R Melin, and Mevin B Hooten. A guide to bayesian model checking for ecologists. *Ecological Monographs*, 88(4):526–542, 2018.
- [14] Paolo Conti, Mengwu Guo, Andrea Manzoni, and Jan S Hesthaven. Multi-fidelity surrogate modeling using long short-term memory networks. *Computer methods in applied mechanics and engineering*, 404, 2023.
- [15] Eric Diehl, Moritz von Tresckow, Lou Scholtissek, Dimitrios Loukrezis, Nicolas Marsic, Wolfgang FO Müller, and Herbert De Gersem. Quadrupole magnet design based on genetic multi-objective optimization. *arXiv preprint arXiv:2211.09580*, 2022.
- [16] Ciobanu Dumitru and Vasilescu Maria. Advantages and disadvantages of using neural networks for predictions. *Ovidius University Annals, Series Economic Sciences*, 13(1), 2013.
- [17] M Giselle Fernández-Godino, Chanyoung Park, Nam-Ho Kim, and Raphael T Haftka. Review of multi-fidelity models. *arXiv preprint arXiv:1609.07196*, 2016.
- [18] Armin Galetzka, Dimitrios Loukrezis, and Herbert De Gersem. Data-driven solvers for strongly nonlinear material response. *International Journal for Numerical Methods in Engineering*, 122(6):1538–1562, 2021.
- [19] P Gardner, TJ Rogers, C Lord, and RJ Barthorpe. Learning model discrepancy: A gaussian process and sampling-based approach. *Mechanical Systems and Signal Processing*, 152:107381, 2021.
- [20] Christophe Geuzaine and Jean-François Remacle. Gmsh: A 3-d finite element mesh generator with built-in pre-and post-processing facilities. *International journal for numerical methods in engineering*, 79(11):1309–1331, 2009.
- [21] Mengwu Guo, Andrea Manzoni, Maurice Amendt, Paolo Conti, and Jan S Hesthaven. Multi-fidelity regression using artificial neural networks: Efficient approximation of parameter-dependent output quan-

ties. *Computer methods in applied mechanics and engineering*, 389:114378, 2022.

- [22] Jiequn Han, Arnulf Jentzen, and Weinan E. Solving high-dimensional partial differential equations using deep learning. *Proceedings of the National Academy of Sciences*, 115(34):8505–8510, 2018.
- [23] Adi Hanuka, Xiaobiao Huang, Jane Shtalenkova, Dylan Kennedy, Aurallee Edelen, Z Zhang, VR Lalchand, D Ratner, and J Duris. Physics model-informed gaussian process for online optimization of particle accelerators. *Physical Review Accelerators and Beams*, 24(7):072802, 2021.
- [24] Jonathan Heek, Anselm Levskaya, Avital Oliver, Marvin Ritter, Bertrand Rondepierre, Andreas Steiner, and Marc van Zee. Flax: A neural network library and ecosystem for JAX, 2023.
- [25] Sepp Hochreiter and Jürgen Schmidhuber. Long short-term memory. *Neural computation*, 9(8):1735–1780, 1997.
- [26] Kwok-Wai Hung and Wan-Chi Siu. Fast video interpolation/upsampling using linear motion model. In *2011 18th IEEE International Conference on Image Processing*, pages 1341–1344. IEEE, 2011.
- [27] Ion Gabriel Ion, Melvin Liebsch, Abele Simona, Dimitrios Loukrezis, Carlo Petrone, Stephan Russenschuck, Herbert De Gersem, and Sebastian Schöps. Local field reconstruction from rotating coil measurements in particle accelerator magnets. *Nuclear Instruments and Methods in Physics Research Section A: Accelerators, Spectrometers, Detectors and Associated Equipment*, 1011:165580, 2021.
- [28] NS Johnson, PS Vulimiri, AC To, X Zhang, CA Brice, BB Kappes, and AP Stebner. Invited review: Machine learning for materials developments in metals additive manufacturing. *Additive Manufacturing*, 36:101641, 2020.
- [29] George Em Karniadakis, Ioannis G Kevrekidis, Lu Lu, Paris Perdikaris, Sifan Wang, and Liu Yang. Physics-informed machine learning. *Nature Reviews Physics*, 3(6):422–440, 2021.

- [30] Karthik Kashinath, M Mustafa, Adrian Albert, JL Wu, C Jiang, Soheil Esmaeilzadeh, Kamyar Azizzadenesheli, R Wang, A Chattopadhyay, A Singh, et al. Physics-informed machine learning: case studies for weather and climate modelling. *Philosophical Transactions of the Royal Society A*, 379(2194):20200093, 2021.
- [31] Ladislav Kavan, Dan Gerszewski, Adam W Bargteil, and Peter-Pike Sloan. Physics-inspired upsampling for cloth simulation in games. In *ACM SIGGRAPH 2011 papers*, pages 1–10. 2011.
- [32] Marc C Kennedy and Anthony O’Hagan. Predicting the output from a complex computer code when fast approximations are available. *Biometrika*, 87(1):1–13, 2000.
- [33] Trenton Kirchdoerfer and Michael Ortiz. Data-driven computational mechanics. *Computer Methods in Applied Mechanics and Engineering*, 304:81–101, 2016.
- [34] Stefan Kurz, Herbert De Gersem, Armin Galetzka, Andreas Klaedtke, Melvin Liebsch, Dimitrios Loukrezis, Stephan Russenschuck, and Manuel Schmidt. Hybrid modeling: towards the next level of scientific computing in engineering. *Journal of Mathematics in Industry*, 12(1):1–12, 2022.
- [35] Dirk Langemann, Cordula Reisch, and Ulrich Römer. Model certification problem for processes. *IFAC-PapersOnLine*, 55(20):193–198, 2022.
- [36] David J Lary, LA Remer, Devon MacNeill, Bryan Roscoe, and Susan Paradise. Machine learning and bias correction of modis aerosol optical depth. *IEEE Geoscience and Remote Sensing Letters*, 6(4):694–698, 2009.
- [37] Matthew Levine and Andrew Stuart. A framework for machine learning of model error in dynamical systems. *Communications of the American Mathematical Society*, 2(07):283–344, 2022.
- [38] Wei Li, Shishi Chen, Zhen Jiang, Daniel W Apley, Zhenzhou Lu, and Wei Chen. Integrating bayesian calibration, bias correction, and machine learning for the 2014 sandia verification and validation challenge problem. *Journal of Verification, Validation and Uncertainty Quantification*, 1(1), 2016.

- [39] A. Logg, K.-A. Mardal, G. N. Wells, et al. *Automated Solution of Differential Equations by the Finite Element Method*. Springer, 2012.
- [40] Sankaran Mahadevan and Ramesh Rebba. Inclusion of model errors in reliability-based optimization. *Journal of Mechanical Design*, 2006.
- [41] Andreas Maier, Harald Köstler, Marco Heisig, Patrick Krauss, and Seung Hee Yang. Known operator learning and hybrid machine learning in medical imaging—a review of the past, the present, and the future. *Progress in Biomedical Engineering*, 2022.
- [42] Stéphane Mallat. Understanding deep convolutional networks. *Philosophical Transactions of the Royal Society A: Mathematical, Physical and Engineering Sciences*, 374(2065):20150203, 2016.
- [43] Stefano Markidis. The old and the new: Can physics-informed deep-learning replace traditional linear solvers? *Frontiers in big Data*, page 92, 2021.
- [44] Karl Mason and Santiago Grijalva. A review of reinforcement learning for autonomous building energy management. *Computers & Electrical Engineering*, 78:300–312, 2019.
- [45] Sanaz Moghim and Rafael L Bras. Bias correction of climate modeled temperature and precipitation using artificial neural networks. *Journal of Hydrometeorology*, 18(7):1867–1884, 2017.
- [46] William L Oberkampf and Christopher J Roy. *Verification and validation in scientific computing*. Cambridge University Press, 2010.
- [47] OpenAI. Gpt-4 technical report, 2023.
- [48] Chanyoung Park, Raphael T Haftka, and Nam H Kim. Remarks on multi-fidelity surrogates. *Structural and Multidisciplinary Optimization*, 55:1029–1050, 2017.
- [49] Lucia Parussini, Daniele Venturi, Paris Perdikaris, and George E Karniadakis. Multi-fidelity gaussian process regression for prediction of random fields. *Journal of Computational Physics*, 336:36–50, 2017.

- [50] Benjamin Peherstorfer, Karen Willcox, and Max Gunzburger. Survey of multifidelity methods in uncertainty propagation, inference, and optimization. *Siam Review*, 60(3):550–591, 2018.
- [51] Jordi Pons, Santiago Pascual, Giulio Cengarle, and Joan Serrà. Upsampling artifacts in neural audio synthesis. In *ICASSP 2021-2021 IEEE International Conference on Acoustics, Speech and Signal Processing (ICASSP)*, pages 3005–3009. IEEE, 2021.
- [52] Alfio Quarteroni and Alberto Valli. *Numerical approximation of partial differential equations*, volume 23. Springer Science & Business Media, 2008.
- [53] Maziar Raissi, Paris Perdikaris, and George E Karniadakis. Physics-informed neural networks: A deep learning framework for solving forward and inverse problems involving nonlinear partial differential equations. *Journal of Computational physics*, 378:686–707, 2019.
- [54] Patrick J Roache. *Verification and validation in computational science and engineering*, volume 895. Hermosa Albuquerque, NM, 1998.
- [55] Christopher Roy and William Oberkampf. A complete framework for verification, validation, and uncertainty quantification in scientific computing. In *48th AIAA Aerospace Sciences Meeting Including the New Horizons Forum and Aerospace Exposition*, page 124, 2010.
- [56] Ahmad EL Sallab, Mohammed Abdou, Etienne Perot, and Senthil Yogamani. Deep reinforcement learning framework for autonomous driving. *arXiv preprint arXiv:1704.02532*, 2017.
- [57] M. W. Scroggs, I. A. Baratta, C. N. Richardson, and G. N. Wells. Basix: a runtime finite element basis evaluation library. *Journal of Open Source Software*, 7(73):3982, 2022.
- [58] M. W. Scroggs, J. S. Dokken, C. N. Richardson, and G. N. Wells. Construction of arbitrary order finite element degree-of-freedom maps on polygonal and polyhedral cell meshes. *ACM Transactions on Mathematical Software*, 48(2):18:1–18:23, 2022.
- [59] Yuwei Shi and John Herniman. The role of expectation in innovation evolution: Exploring hype cycles. *Technovation*, 119:102459, 2023.

- [60] Gilbert Strang. Variational crimes in the finite element method. In *The mathematical foundations of the finite element method with applications to partial differential equations*, pages 689–710. Elsevier, 1972.
- [61] Kiwon Um, Robert Brand, Philipp Holl, Nils Thuerey, et al. Solver-in-the-loop: Learning from differentiable physics to interact with iterative pde-solvers. *arXiv preprint arXiv:2007.00016*, 2020.
- [62] Shashank Reddy Vadyala, Sai Nethra Betgeri, John C Matthews, and Elizabeth Matthews. A review of physics-based machine learning in civil engineering. *Results in Engineering*, 13:100316, 2022.
- [63] Fang Wang and Di Tian. On deep learning-based bias correction and downscaling of multiple climate models simulations. *Climate dynamics*, 59(11-12):3451–3468, 2022.
- [64] Shuchun Wang, Wei Chen, and Kwok-Leung Tsui. Bayesian validation of computer models. *Technometrics*, 51(4):439–451, 2009.
- [65] Christopher KI Williams and Carl Edward Rasmussen. *Gaussian processes for machine learning*, volume 2. MIT press Cambridge, MA, 2006.
- [66] Zonghan Wu, Shirui Pan, Fengwen Chen, Guodong Long, Chengqi Zhang, and Philip S. Yu. A comprehensive survey on graph neural networks. *IEEE Transactions on Neural Networks and Learning Systems*, 32(1):4–24, 2021.
- [67] Samir S Yadav and Shivajirao M Jadhav. Deep convolutional neural network based medical image classification for disease diagnosis. *Journal of Big data*, 6(1):1–18, 2019.